Probabilistic Tsunami Damage Assessment Considering Stochastic Source Models: Application to the 2011 Tohoku Earthquake

Katsuichiro Goda[1], Shiliang Li[2], Nobuhito Mori[3], and Tomohiro Yasuda[4]

[1]Senior Lecturer, Department of Civil Engineering, Queen's School of Engineering, University of Bristol, Queen's Building, University Walk, Bristol, BS8 1TR, United Kingdom

[2]PhD Candidate, Department of Civil Engineering, Queen's School of Engineering, University of Bristol, Queen's Building, University Walk, Bristol, BS8 1TR, United Kingdom

[3]Associate Professor, Disaster Prevention Research Institute, Kyoto University, Gokasho, Uji, Kyoto 611-0011, Japan

[4]Assisstant Professor, Disaster Prevention Research Institute, Kyoto University, Gokasho, Uji, Kyoto 611-0011, Japan

Submitted to:

Coastal Engineering Journal

Corresponding author:

Katsuichiro Goda

E-mail: katsu.goda@bristol.ac.uk

Abstract

A computational framework for probabilistic tsunami risk assessment due to a mega-thrust subduction earthquake is developed and is applied to the 2011 Tohoku Tsunami from retrospective viewpoints. The uncertain tsunami source characteristics are represented by multiple source inversion models and their stochastic variations that are generated using the spectral analysis and synthesis method. By conducting Monte Carlo tsunami simulation, stochastic inundation depth maps can be developed, which are subsequently integrated with tsunami fragility curves to develop stochastic tsunami risk maps. The stochastic tsunami risk maps display spatial variability of tsunami damage probabilities for a building portfolio, reflecting not only possible tsunami scenarios but also uncertain tsunami resistance of buildings. The numerical results indicate that both stochastic tsunami risk maps and risk curves are affected by the local terrain features, proximity to major tsunami sources, and building characteristics (material type and story number). Consideration of different reference tsunami source models in probabilistic tsunami risk assessment are identified as one of the critical contributors to the overall uncertainty of the tsunami risk predictions. Therefore, in determining critical scenarios for tsunami evacuation and risk mitigation, a wide range of possible tsunami scenarios should be considered in light of the current limited seismological knowledge for the mega-thrust subduction earthquake.

Key words: Tsunami risk, Uncertainty, Stochastic earthquake source modeling, Tsunami fragility, 2011 Tohoku Tsunami

41 ## 1. Introduction

42 Tsunami risk due to large subduction earthquakes is catastrophic and is highly uncertain.
43 Devastating tsunami disasters that struck in the last decade include the 2004 Indian Ocean tsunami
44 (Borrero, 2005; Murata et al., 2010) and the 2011 Great East Japan (Tohoku) tsunami (Fraser et al.,
45 2013; Suppasri et al., 2013b). The potential impact of giant tsunamis is calamitous, causing
46 tremendous fatalities (tens to hundreds of thousands), massive damage to structures and
47 infrastructure (hundreds of thousands of houses and buildings, affecting/displacing millions of
48 people), and huge economic loss (tens to hundreds of billion dollars). To mitigate such negative
49 impact, protection and preparedness against tsunami disasters need to be improved by combining
50 hard and soft measures effectively (FEMA, 2008; Murata et al., 2010). The hard measures include
51 construction of coastal defense structures, such as breakwaters and revetments, and evacuation
52 facilities. On the other hand, soft measures can be implemented through early warning systems,
53 emergency planning, and evacuation drills. Generally, hard and soft measures are complementary,
54 and enhance the tsunami resilience of local coastal communities differently. Because the selection
55 and implementation of hard and soft measures depend on the anticipated tsunami hazard scenarios
56 and their potential consequences, accurate hazard and risk assessment for future catastrophic
57 tsunami events is the key for effective disaster risk reduction (DRR). Once predicted hazards are
58 determined, risk managers in municipalities and central governments need to prepare against
59 forecasted hazards. Therefore, it is critically important to know the severity of potential tsunami
60 risks quantitatively.

61 Major challenges in assessing the tsunami impact are to predict the source characteristics of
62 future tsunamigenic earthquakes (e.g. location, magnitude, and slip distribution) and to quantify the
63 uncertainty associated with the predictions. In particular, earthquake slip distributions and rupture
64 processes have major influence on tsunami wave height and inundation extent (Geist, 2002;
65 McCloskey et al., 2008; Suppasri et al., 2010; Løvholt et al., 2012; Fraser et al., 2014; Goda et al.,

66 2014; Wiebe and Cox, 2014; Fukutani et al., 2015; Mueller et al., 2015). Recent development in
67 probabilistic tsunami hazard analysis (PTHA) and mapping facilitates the generation of stochastic
68 earthquake source models (Mai and Beroza, 2002; Lavallée et al., 2006; Goda et al., 2014), which
69 represent possible scenarios having different earthquake slips and fault geometry. The stochastic
70 method is based on the spectral analysis of slip heterogeneity in the wavenumber domain and
71 implements the spectral synthesis to generate random fields that have realistic slip characteristics,
72 such as asperities. It is useful for quantifying the effects of uncertain source characteristics on
73 tsunami wave profiles and spatial extent of inundation. By conducting Monte Carlo tsunami
74 simulation based on stochastic source models, stochastic inundation depth maps can be evaluated
75 (Goda et al., 2015; Mueller et al., 2015). An advantage of such probabilistic hazard maps is that the
76 main sources of uncertainty related to the tsunami hazard assessment are taken into account,
77 promoting the informed decisions regarding DRR actions by understanding the consequences of
78 different situations (typical scenario versus worst-case scenario) and by communicating the
79 uncertainty associated with hazard predictions (Pang, 2008).

80 It is noteworthy that for risk managers and emergency officers, information related to tsunami
81 risk and potential damage is more relevant, e.g. number of collapsed buildings and number of
82 fatalities in different coastal communities. For such purposes, tsunami fragility, which essentially
83 relates site-specific tsunami hazard information to tsunami risk/damage information of a building, is
84 needed to obtain probabilistic estimates of tsunami risk metrics. A tsunami fragility model evaluates
85 damage probabilities of a class of buildings for a given tsunami hazard parameter (e.g. inundation
86 depth and flow velocity). Various empirical tsunami fragility models have been developed as a
87 function of inundation depth based on post-tsunami field observations, numerical simulation, and
88 satellite images for different regions (Koshimura et al., 2009; Reese et al., 2011; Suppasri et al.,
89 2011; Mas et al., 2012; Tarbotton et al., 2015).

This study investigates the uncertainty propagation of earthquake source characteristics in probabilistic tsunami risk analysis by focusing upon the 2011 Tohoku Tsunami from retrospective viewpoints. The 2011 Tohoku event offers unique opportunities to carry out rigorous tsunami risk assessment, because various data and models for earthquake source properties, inundation/run-up measurements, and tsunami damage records are available in detail. The quality and amount of available information are unprecedented in comparison with other previous events. For instance, reliable tsunami inundation and run-up survey results (more than 5,000 locations) are available from the Tohoku Tsunami Joint Survey (TTJS) team (Mori et al., 2011), whereas tsunami damage data as well as building data for the Tohoku region (more than 250,000 buildings) are available from the Ministry of Land, Infrastructure, and Transportation (MLIT) of Japan. Regarding the earthquake source characteristics of the Tohoku event, various inversion models have been developed in the literature (Ammon et al., 2011; Fujii et al., 2011; Hayes, 2011; Iinuma et al., 2011, 2012; Shao et al., 2011; Yamazaki et al., 2011; Gusman et al., 2012; Satake et al., 2013). Based on these, numerous stochastic source models can be generated, and subsequently, Monte Carlo tsunami simulation can be carried out (Goda et al., 2014). It is important to emphasize that stochastic source models generated in this study are intended to cover a wide range of possible earthquake scenarios that may be applicable to tsunami hazard mapping purposes. Moreover, empirical tsunami fragility models for different building materials and story numbers have been developed using the extensive MLIT tsunami damage database (Suppasri et al., 2013a; Charvet et al., 2014). The tsunami hazard and fragility models are then integrated in probabilistic tsunami risk analysis to investigate the variability of tsunami risk metrics in cities and towns along the Tohoku coast. The tsunami risk metrics that are focused upon in this study are the probabilities and the numbers of buildings for several severe damage states (e.g. *wash-way*, *collapse*, and *complete damage*). The building stock that is considered in the damage assessment (i.e. tsunami risk exposure) is that along the Tohoku coast prior to the 2011 Tohoku event (note: as of 2015, rebuilding processes of local communities

affected by the Tohoku Tsunami are still in progress). A novel aspect of this study is that quantitative tsunami risk assessment is carried out at both municipality and regional levels by accounting for uncertainties in establishing earthquake slip distributions. The results have major implications on tsunami risk management and DRR actions for future giant tsunamis in the Tohoku region.

This study is organized as follows. Section 2 presents an analytical procedure for assessing the tsunami risk and damage of buildings. The section consists of a description of a generic methodology for probabilistic tsunami risk assessment (Section 2.1), stochastic modeling of earthquake slips (Section 2.2), Monte Carlo tsunami simulation (Section 2.3), and tsunami fragility and damage analysis (Section 2.4). Section 3 presents tsunami risk analysis results for the building stock in the Tohoku region. The problem set-up is described in Section 3.1. The assessment is conducted by considering a single reference source model (Section 3.2) as well as multiple reference source models (Section 3.3). The latter accounts for epistemic uncertainty associated with stochastic source modeling. Finally, Section 4 provides the main conclusions of this study.

2. Methodology

2.1 Probabilistic tsunami risk analysis

To assess potential impact of future destructive tsunamis by accounting for uncertainty associated with predictions, probabilistic methods for tsunami damage assessment are essential. Important requirements for a viable methodology for tsunami risk assessment are that key variables and model components, such as earthquake source characteristics, wave propagation, tsunami inundation and run-up, and tsunami vulnerability of structures, are modeled comprehensively and that their uncertainty and dependency are propagated consistently through probabilistic calculus. A similar analytical risk analysis framework that has been developed and implemented for seismic hazard and risk assessment (e.g. McGuire, 2004; Yoshikawa and Goda, 2014) can be adopted for

tsunami risk assessment. This is a viable approach for extending the current PTHA (e.g. Geist and Parsons, 2006; Thio et al., 2007; Horspool et al., 2014) that has many common features with probabilistic seismic hazard analysis (e.g. McGuire, 2004) regarding mathematical formulation and uncertainty modeling.

A generic equation for probabilistic risk analysis can be expressed as:

$$\nu(DS \geq ds) = \iint_{\Omega_{IM,EQS}} P(DS \geq ds|im)\, f_{IM|EQS}(im|eqs)\, f_{EQS}(eqs)|\mathrm{d}im\|\mathrm{d}\lambda(eqs)| \quad (1)$$

where $\nu(DS \geq ds)$ is the annual exceedance probability that the damage state DS of a structure exceeds a certain tsunami damage threshold ds, $\lambda(eqs)$ is the annual occurrence rate of earthquake scenarios (EQS) represented by multiple physical parameters (e.g. magnitude, location, geometry, and slip distribution), $P(DS \geq ds|im)$ is the tsunami vulnerability/fragility function in terms of intensity measure (IM), $f_{IM|EQS}$ is the probability density function of IM given EQS, f_{EQS} is the probability density function of EQS, and $\Omega_{IM,EQS}$ is the joint domain of integration for IM and EQS. A typical IM is the inundation depth, which is often used as an input parameter for tsunami fragility modeling (i.e. $P(DS \geq ds|im)$). In tsunami risk analysis, $f_{IM|EQS}$ is evaluated through numerical evaluations of governing equations for tsunami waves and inundation/run-up (e.g. solving the nonlinear shallow water equations for given initial boundary conditions). The uncertainty associated with variable earthquake source characteristics is captured by f_{EQS}. It is noteworthy that when earthquake scenarios are defined for a single source region or a specific situation (e.g. M_w9-class subduction events off the Tohoku coast), the interpretation of Equation (1) becomes conditional. Such conditional assessment may be considered for situations where dominant earthquake source regions are identified through historical tsunami records or PTHA, but their occurrence probabilities and potential earthquake sizes cannot be estimated reliably (Kagan and Jackson, 2013). A notable advantage of the conditional evaluations is that the nonlinear physical processes of tsunami wave propagation and inundation as well as the uncertainty of detailed source characteristics can be fully

164 incorporated in the hazard computation (Goda et al., 2014, 2015). Ideally, complete tsunami
165 hazard/risk analysis is desirable and should take into account both multiple tsunami sources (having
166 a wide range of earthquake magnitudes as in PTHA) and their variability by evaluating the
167 nonlinear governing equations of tsunami inundation. Nonetheless, at present, it is computationally
168 demanding to achieve this, noting that the majority of the PTHA methods are formulated based on
169 the superposition of the linear solutions of the governing equations at near-shore locations with
170 relatively shallow depths (Geist and Parsons, 2006; Thio et al., 2007; Horspool et al., 2014).

171 This study aims at assessing the tsunami damage to the building stock in the Tohoku region
172 for M_w9-class mega-thrust interface subduction earthquakes. This corresponds to the conditional
173 evaluation of Equation (1), ignoring other distant sources (e.g. tsunamis from Chile). The
174 assessment takes into account a range of variable source characteristics of the earthquakes (i.e. fault
175 geometry and slip distribution), which should contain unexpected or extreme events. The
176 consideration of stochastic earthquake source models in Monte Carlo tsunami simulation and
177 probabilistic tsunami damage assessment is novel. Essentially, this means that uncertainty of initial
178 boundary conditions for tsunami modeling is propagated through dynamical fluid systems and
179 causal tsunami vulnerability relationships for buildings. Such investigations are useful for assessing
180 the sensitivity and variability of tsunami hazard parameters and tsunami risk/damage metrics at both
181 local and regional scales and for hazard mapping, risk communication, and emergency preparedness.
182 Based on the scope of this study, a computational procedure for carrying probabilistic tsunami risk
183 assessment for buildings in coastal environments is presented in Figure 1. It consists of several
184 major modules: stochastic source modeling, tsunami simulation, exposure modeling (i.e. building
185 data), and tsunami vulnerability assessment. Salient features of these model components are
186 described in Sections 2.2 to 2.4.
187
188

2.2 Stochastic source models

An earthquake slip modeling procedure, which is based on spectral analysis of an inversion-based source model and spectral synthesis of random fields, generates earthquake slip distributions with statistical properties equivalent to the inverted source model. The method is based on Mai and Beroza (2002), and has been modified for large mega-thrust subduction earthquakes (Goda et al., 2014). The random-field generation method is designed to balance similarity in key features of the inversion-based models (e.g. overall slip distribution and its spectral characteristics) with dissimilarity of fine details (e.g. locations of large slip patches). A brief summary of the stochastic method is given in Section 2.2.1.

It is important to recognize that the generated stochastic source models are dependent on the source characteristics of the reference model that is derived from inversion analysis. Because data and methods used for constraining the slip distribution over a fault plane differ significantly, details of the slip distribution and fault geometry differ significantly among the inversion models. This reflects the complexity and uncertainty of the rupture process of mega-thrust subduction earthquakes. Therefore, to explore a range of possible slip distributions for a given scenario, multiple reference models should be considered for generating stochastic source models. Key features of the inverted source models for the 2011 Tohoku earthquake, which are adopted for stochastic source modeling in this study, are described in Section 2.2.2. The reference models that are adopted for the stochastic source modeling in Section 2.2.2 are assigned with equal weights. This equal weighting can be changed if specific preferences are given to some of the reference models (e.g. those based on tsunami inversion). Unequal weighing is not considered in this study because the study is aimed at capturing a wide range of slip distributions based on different geophysical data and source inversion methods and a priori performance tests of candidate models are not always feasible to perform.

214 2.2.1 *Spectral synthesis of earthquake slip distribution*

215 A graphical flowchart of the random-field generation procedure is shown in Figures 2, 3, and
216 4; an example shown in the figure is for an inversion model by Satake et al. (2013).

217 Prior to spectral analysis, an original slip model needs modifications (STEP 1; Figure 2). An
218 original slip model is read as a cell-based distribution; in this step, an asperity zone, which is used
219 for pattern matching in spectral synthesis, is identified (STEP 1-1). Typically, the asperity zone is
220 defined as a set of sub-faults that have slip values greater than a specified threshold value. Typically,
221 the threshold is set to two to three times the average slip (Mai et al., 2005). One of the key features
222 of the slip models for the 2011 Tohoku earthquake is that very large slip values (e.g. exceeding 40
223 m) are obtained for a small number of sub-faults (Goda et al., 2014). This results in slip
224 distributions that are significantly different from the normal distribution and exhibit a heavy right-
225 tail feature (in comparison with the normal distribution with the same statistics; see STEP 1-2). This
226 can cause problems in stochastic simulation of slip distributions because the random-field method
227 implemented in this study (Pardo-Iguzquiza and Chica-Olmo, 1993) generates slip distributions
228 with quasi-normal slip values over a fault plane. To deal with non-normal slip distribution,
229 nonlinear scaling of the slip values is considered in the random-field generation procedure. To
230 identify a suitable nonlinear scaling method, in STEP 1-2, characteristics of the slip distribution are
231 analyzed using the Box–Cox transformation, in which an original variable x (i.e. non-normal slip
232 values) is converted into y as: $y = (x^{\lambda}-1)/\lambda$. The method identifies the best power transformation
233 parameter λ by maximizing the linear correlation coefficient between the standard normal variate
234 and the transformed variable y for different values of λ. For the Satake et al. model, an optimal
235 value of λ is estimated as 0.2 (STEP 1-2). The obtained value of λ is used to perform nonlinear
236 scaling of the synthesized slip distributions in spectral synthesis (i.e. inverse Box–Cox
237 transformation; STEP 3-2). Subsequently, the cell-based model is converted to a grid-based model
238 and interpolated bilinearly, and is then tapered such that slip decreases to zero to each side of the

fault plane to achieve smooth transition at the fault boundary (STEP 1-3). The grid spacing for interpolation is selected according to the grid size of the original slip model.

Using the interpolated and tapered slip distribution in STEP 1, fast Fourier transform (FFT) of the slip distribution is carried out to obtain the two-dimensional (2D) normalized power spectrum (STEP 2-1; Figure 3). Usable wavenumber ranges are determined based on the characteristic dimension of the fault plane for the lower limit and the spatial resolution of the original slip model for the upper limit. The extracted normalized power spectra in the down-dip and along-strike directions are fitted by the power spectrum of a theoretical auto-correlation function (STEP 2-2). In this study, the power spectrum $P(k)$ of an anisotropic von Kármán auto-correlation function is considered:

$$P(k) \propto \frac{A_x A_z}{(1+k^2)^{H+1}}, \tag{2}$$

where k is the wavenumber, $k = (A_z^2 k_z^2 + A_x^2 k_x^2)^{0.5}$, A_z and A_x are the correlation lengths for the down-dip and along-strike directions, respectively, and H is the Hurst number. At wavenumber scales greater than the correlation length, the slip distribution is mainly governed by the average slip characteristics (with randomness represented by white noises), whereas at wavenumber scales less than the correlation length, local heterogeneity dominates. A_x and A_z control the absolute level of the power spectrum in the low wavenumber range (i.e. $k << 1$) and capture the anisotropic spectral features of the slip distribution. H determines the slope of the power spectral decay in the high wavenumber range, and theoretically is constrained to fall between 0 and 1. For the Satake et al. model, A_x and A_z are estimated as 56 km and 107 km, respectively, whereas $H = 0.82$ is obtained.

In STEP 3 (Figure 4), multiple realizations of slip distributions with desired stochastic properties are obtained. In STEP 3-1, a random field, having quasi-normal distribution with a desired spatial correlation structure, is synthesized using a Fourier integral method (Pardo-Iguzquiza and Chica-Olmo, 1993). The amplitude spectrum of the target slip distribution is specified by the theoretical power spectrum with the correlation lengths and Hurst number that are

264 estimated in STEP 2, while the phase spectrum is represented by a random phase matrix. The
265 constructed complex Fourier coefficients are transformed into the spatial domain via 2D inverse
266 FFT. The synthesized slip distribution is then scaled nonlinearly to have heavy right-tail
267 characteristics using the Box–Cox parameter λ estimated in STEP 1-2 (STEP 3-2). In this
268 manipulation, an upper bound (i.e. maximum slip of the original model) is implemented for the
269 transformed slip distribution to avoid unrealistically large slip.

270 To resemble the synthesized slip distribution with the original one in terms of location and
271 amplitude of asperities, a rectangular asperity zone is defined for the synthesized slip distribution,
272 and then compared with the original slip distribution. The asperity dimensions of the synthesized
273 distribution are specified by fractions of fault length and width, whereas the extent of the slip
274 concentration around the asperity is specified by a percentage of slip within the asperity zone with
275 respect to the total sum of slip over the fault plane. Parameters of the rectangular asperity zone are
276 determined based on the original slip model. For the Satake et al. model, the dimensions of the
277 asperity zone are set to 50 km and 220 km for the down-dip and along-strike directions, respectively
278 (in terms of fault dimensions, these correspond to fractional factors of 0.25 and 0.4, respectively),
279 whereas the slip concentration ratio of 0.3 is considered. These parameters approximately resemble
280 the asperity zone that is identified for the original slip distribution (STEP 1-1). An acceptable slip
281 distribution is required to have its maximum slip patch within the asperity zone of the original
282 distribution. The criterion for acceptance is set as follows: the simulated slip distribution has a
283 major asperity (i.e. slip concentration located in the rectangular asperity zone) that exceeds a
284 threshold defined based on the original slip distribution (see Table 1; STEP 3-3). To ensure this
285 requirement, multiple realizations are generated (STEP 3-4). Finally, the mean and standard
286 deviation of the transformed slip distribution are adjusted to achieve similar statistics of the
287 synthesized slip model with regard to the original slip model; this means that the seismic moments
288 of the simulated slip distribution and the reference source model are similar.

289 2.2.2 *Inverted source models and variations of source properties*

290 Multiple inversion models for the 2011 Tohoku Tsunami are gathered from the literature. In
291 total, eleven source models that are developed using teleseismic/tsunami/geodetic data are
292 considered (Ammon et al., 2011; Fujii et al., 2011; Hayes, 2011; Iinuma et al., 2011, 2012; Shao et
293 al., 2011; Yamazaki et al., 2011; Gusman et al., 2012; Satake et al., 2013), and are used as reference
294 to further produce models with variable source characteristics. Figure 5 shows the eleven source
295 models, and Table 1 summarizes their key features. In Figure 5, regions outlined by thick black
296 lines represent the asperity area, slip of which is equal to or greater than three times the average slip.
297 The moment magnitudes of the source models range from 8.97 to 9.14, which translate into a factor
298 of 1.8 difference in seismic moment. Notable differences in slip models are observed in terms of
299 fault plane dimensions, as well as location and concentration of large slip patches. The fault length
300 varies from 340 km to 625 km, while the fault width ranges from 200 km to 260 km. The depth to
301 the top-edge of the fault plane varies from 0 km to 7.4 km, while the fault strike falls between 192º
302 to 202º, approximately parallel to the Japan Trench. Models 1, 3 to 7, and 9 assume constant dip
303 (between 10º and 14º), whereas other models have variable dip angles that gradually steepen with
304 increasing depth. The rake angles vary slightly, representing reverse fault mechanisms (near 90º).
305 The characteristics of slip asperities, such as location, size, shape, and amplitude, differ
306 significantly among the inversion models. Models 2, 6, and 11 have large asperities along the
307 eastern edge of the fault plane, while others have large slip values near the epicenter. The maximum
308 slip values for the eleven models range from 35 m to 75 m. Models 3, 5, and 7 are characterized by
309 slip concentration extending primarily along strike, whereas models 1, 4, and 8 have circular/elliptic
310 slip concentration.

311 To generate source models that have different geometrical properties from the reference
312 models, the top-edge depth, strike, and dip are varied over certain ranges with respect to the original
313 models by changing one parameter at a time and by keeping a slip distribution identical to the

original model. The ranges of geometrical parameters are chosen based on the seismotectonic setting in the Tohoku region. Geometrical parameters are allowed to vary as follows: the top-edge depth varies in steps of 2.5 km from by -2.5 km to +10 km with respect to the reference depth; the strike angle takes on values between -5º and +7.5º in 2.5º increment with respect to the reference strike; the dip angle is changed between -5º and +10.0º in 2.5º increment from the reference dip. When parameters of an original source model are variable, an average value is used to define a reference case for each parameter.

Moreover, 50 realizations of a target slip distribution are generated for each of the eleven original models using the stochastic synthesis method (Section 2.2.1) by keeping their geometrical parameters identical to those of the original models. Table 1 also lists the stochastic slip parameters that are relevant to random-field generation. The von Kármán parameters, A_z, A_x, and H, characterize the spatial heterogeneity of stochastic earthquake slip. All Hurst numbers but two (models 2 and 6) are set to 0.99 to constrain this parameter within a physically meaningful range (i.e. $H < 1.0$). When $A_x > A_z$, the slip distribution is more coherent in along-strike direction, thereby capturing anisotropic features of the slip distributions. All Box–Cox parameters, except for model 11, are positive (between 0.1 and 0.3), indicating that the right-tail characteristics of the slip models 1 to 10 are less heavy than the logarithmic case. The heavy right-tail feature of model 11 ($\lambda = 0.0$) is attributed to very large slip values (exceeding 70 m) for several sub-faults along the Trench (see Figure 5). The fractional values for size and slip concentration of the asperity zone capture key features of asperities, and are subsequently used to determine acceptance/rejection for synthesized slip distributions. Typically, 25% to 45% of total slips are concentrated in about 9% to 13% of the fault plane areas.

In total, 726 slip distributions are generated for Monte Carlo tsunami simulation (66 cases per reference model, consisting of a reference case, 15 cases with varied geometrical parameters, and 50 cases with stochastic slip distributions).

339 ## 2.3 Monte Carlo tsunami simulation

340 Tsunami modeling is carried out using a well-tested numerical code (Goto et al., 1997) that is
341 capable of generating off-shore tsunami propagation and inundation/run-up by evaluating nonlinear
342 shallow water equations using a leap-frog staggered-grid finite difference scheme. The
343 inundation/run-up calculation is performed by a moving boundary approach, where a dry/wet
344 condition of a computational cell is determined based on total water depth. The computational
345 domains are nested at four resolutions (i.e. 1350-m, 450-m, 150-m, and 50-m domains).
346 Computational cells include those on land, and coastal defense structures are taken into account
347 using Homma's overflowing formulae as a sub-grid model.

348 Bathymetry/elevation data, roughness/friction coefficient data, and information of coastal
349 defense structures for the Tohoku region are obtained from the Cabinet Office of the Japanese
350 Government. The ocean bathymetry data are based on the digital bathymetry data and nautical
351 charts developed by Japan Hydrographic Association and Japan Coastal Guard. The land elevation
352 data are based on the 50-m grid digital elevation model (DEM) developed by the Geospatial
353 Information Authority of Japan. The raw data are the standard 1:25,000 topographical map of Japan
354 and are obtained from aerial photographic surveys. The grid resolution of 50 m is not sufficiently
355 fine to represent major infrastructures, such as highway embankments. It is also noted that the 50-m
356 grid DEM data, which only represent an average value for a given cell, are rough approximations of
357 the elevations at individual sites. The bottom friction is evaluated using Manning's formula. Four
358 Manning's coefficients are assigned to computational cells based on national land use data in Japan
359 (100-m mesh): 0.02 $m^{-1/3}s$ for agricultural land, 0.025 $m^{-1/3}s$ for ocean/water, 0.03 $m^{-1/3}s$ for forest
360 vegetation, and 0.04 $m^{-1/3}s$ for urban areas. The roughness coefficients that are used in the analyses
361 may be considered to be low in light of other studies on tsunami and storm surge inundation. For
362 example, roughness coefficients of 0.05 to 0.2 $m^{-1/3}s$ are indicated for urban areas and forest
363 vegetation (Bunya et al., 2010; Kaiser et al., 2011). Preliminary analyses, which are conducted by

364 considering the roughness coefficients of 0.09 $m^{-1/3}s$ and 0.12 $m^{-1/3}s$ for urban and forest areas,
365 respectively, indicate that the effects of greater roughness coefficients are noticeable in coastal plain
366 regions, reducing the inundation extent, whereas those in ria coastal regions are relatively minor.
367 Nevertheless, in this study, alternative sets of roughness coefficient are not considered (beyond the
368 scope of this study); such investigations should be conducted in the future. The results shown in
369 Section 3 should be interpreted based on the assumed values of roughness coefficient (which may
370 lead to overestimation of inundation extent).

371 Differences in earthquake slip result in different boundary conditions for tsunami propagation
372 and inundation/run-up. In tsunami simulation, the vertical seafloor displacement is directly taken as
373 the initial water surface elevation, which can be evaluated based on formulae by Okada (1985) and
374 Tanioka and Satake (1996). The latter equation accounts for the effects of horizontal seafloor
375 movements in case of steep seafloor, inducing additional vertical water dislocation. Although the
376 seafloor deformations are obtained for the same event, spatial characteristics of the seafloor
377 displacements vary significantly among the models, leading to various tsunami wave profiles at
378 different locations along the Tohoku coast (Goda et al., 2014). The fault rupture is assumed to occur
379 instantaneously, and numerical tsunami calculation is performed for duration of 2 hours with an
380 integration time step of 0.5 s.

381 The tsunami simulation is performed for the 726 source models (Section 2.2.2). For each case,
382 the maximum inundation depths at all in-land computational cells (50-m grids) are obtained by
383 subtracting the DEM data from the calculated maximum wave heights. The computational region
384 covers from Miyako in Iwate Prefecture to Soma in Fukushima Prefecture. Figure 6 shows a map of
385 the Tohoku region, displaying the locations of coastal cities and towns that are focused upon in this
386 study. Geographically, there are two main coastal features: the Sanriku ria coast in the northern
387 Tohoku region (Onagawa to Miyako) and the Sendai coastal plain in the southern Tohoku region
388 (Soma to Ishinomaki). Due to narrow submerged valleys along the Sanriku ria coast, tsunami waves

389 tend to be amplified significantly; thus inundation depth and run-up height are often much greater at
390 locations along the Sanriku ria coast, in comparison with locations in the Sendai plain. On the other
391 hand, the spatial extent of inundation in the Sendai plain is much greater than that in the Sanriku
392 coast, due to its low-lying terrain.

393 It is instructive to demonstrate that the tsunami simulation using source models based on
394 tsunami inversion (e.g. Fujii et al., 2011; Gusman et al., 2012; Satake et al., 2013) can produce
395 inundation depths similar to the observed inundation depths during the 2011 Tohoku event (note:
396 inundation and run-up data are not used directly in inversion analysis). For this purpose, simulated
397 inundation depth contours based on the Satake et al. source model are compared in Figure 7 with
398 the observed inundation depths based on the TTJS database for three representative locations, i.e.
399 Kamaishi, Onagawa, and Sendai-Natori-Iwanuma (see also Figure 6 for the maximum wave height
400 contour). The first two are positioned in the Sanriku ria coast, whereas the latter is located in the
401 Sendai coastal plain (Figure 6). Since the large slip patches and epicenter are located off northern
402 Miyagi Prefecture (Figure 5), the tsunami wave propagation from the source region for Kamaishi
403 and Onagawa differs. In Figure 7a, contour maps are based on the tsunami simulation, whereas
404 color-coded markers show the TTJS data (note: similar color schemes are adopted for the
405 simulation results and the TTJS data to facilitate the visual comparison). Figure 7b compares the
406 results in the scatter plot format. Generally, the inundation depths as well as spatial footprints based
407 on the Satake et al. model are consistent with the observed inundation data. However, at some
408 locations (Figure 7b), the observations and the simulated inundation depths differ significantly. The
409 major reasons for the differences are: (i) the source model is not perfect; (ii) 50-m grid resolution
410 for the DEM, roughness, and coastal data is inaccurate for individual locations; (iii) some of the
411 major coastal structures are not represented completely (e.g. Kamaishi deep breakwater and Sendai
412 Tobu highway); (iv) the post-event observations include bias due to local effects; and (v) other
413 limitations (e.g. incorrect roughness coefficients for the actual land use). More detailed, quantitative

414 comparisons between the tsunami simulation results based on various source models (not only
415 reference models but also stochastic source models) and the actual observations are discussed in
416 Goda et al. (2015).
417
418 **2.4 Tsunami fragility and damage analysis**
419 Structural vulnerability/fragility against tsunami loading is an essential component for
420 tsunami risk and damage assessment. This can be modeled by empirical tsunami fragility curves,
421 which relate tsunami intensity measures (*IM*) to tsunami damage states (*DS*) statistically. The
422 damage states of structures are determined during reconnaissance survey and building inspection.
423 Typical parameters for *IM* are the inundation depth and the flow velocity; the former is more
424 frequently considered because the inundation depth is usually observable by post-event surveys and
425 its estimation is more reliable than the flow velocity (e.g. water marks, post-tsunami interview, and
426 numerical simulation). It is important to recognize that both *IM* and *DS* are subject to errors and
427 uncertainty. From a structural reliability viewpoint, fragility curves represent the conditional
428 structural capacity models for different limit states, and thus it is desirable to develop separate
429 fragility models for structures having different tsunami resistances.
430 Mathematically, the tsunami fragility is often approximated by the lognormal distribution.
431 The exceedance probability of the i-th damage state ds_i for a given value *im* is expressed as:

432 $$P(DS \geq ds_i | im) = \Phi\left(\frac{\ln(im) - \mu_{\ln IM|DS_i}}{\sigma_{\ln IM|DS_i}}\right) \quad (3)$$

433 where Φ is the cumulative distribution function of the standard normal variate, and $\mu_{\ln IM|DS_i}$ and
434 $\sigma_{\ln IM|DS_i}$ are the mean and standard deviation of $\ln IM|DS_i$, respectively. The fragility model
435 parameters $\mu_{\ln IM|DS_i}$ and $\sigma_{\ln IM|DS_i}$ can be estimated via regression analysis of the tsunami damage data.
436 As the damage states are mutually exclusive, the probability of being in the damage state ds_i can be
437 evaluated by:

438 $$p(DS = ds_i | im) = P(DS \geq ds_i | im) - P(DS \geq ds_{i+1} | im) \quad (4)$$

439 Note that ds_{i+1} is severer than ds_i (i.e. $P(DS \geq ds_{i+1}|im) < P(DS \geq ds_i|im)$).

440 In Japan, the MLIT (2014) implements a uniform classification scheme for tsunami damage
441 survey for the 2011 Tohoku Tsunami. Seven damage levels are defined: *no damage*, *minor damage*,
442 *moderate damage*, *major damage*, *complete damage*, *collapse*, and *wash-away*. Furthermore,
443 information regarding the structural material types and the number of stories is also provided. The
444 material types are categorized into: reinforced concrete (RC), steel, wood, masonry, and unknown,
445 whereas the number of stories is divided into: 1-story, 2-story, and 3+-story. The supplementary
446 data are useful in developing fragility models for buildings with different capacities, because these
447 structural characteristics have significant influence on the fragility curves (Koshimura et al., 2009;
448 Reese et al., 2011; Suppasri et al., 2011, 2013a; Charvet et al., 2014).

449 Using the extensive MLIT tsunami damage database for the 2011 Tohoku Tsunami (more
450 than 250,000 data points), Suppasri et al. (2013a) developed eleven sets of fragility models for
451 different material types (note: each set consists of six fragility curves for the six damage states
452 excluding *no damage*). There are three levels of the data classification and model development. The
453 level-1 models (crudest) develop a set of fragility curves using all data. The level-2 models
454 (intermediate) distinguish tsunami damage data according to the structural materials and develop
455 four sets of fragility curves for RC, steel, wood, and masonry. The level-3 models (refined) further
456 divide the data for RC and wood structures according to the number of stories, and develop six sets
457 of fragility curves for RC-1-story, RC-2-story, RC-3+-story, wood-1-story, wood-2-story, and
458 wood-3+-story. The refinement for the different material types as well as for the number of stories
459 is desirable, because the tsunami capacities for RC, steel, wood, and masonry buildings differ
460 significantly. Generally, the fragility models by Suppasri et al. (2013a) are applicable to the entire
461 Tohoku region; however, at local levels, the models may produce biased predictions because some
462 of the local features that affect tsunami damage are not captured. In this regard, using more

463 elaborated models that incorporate local features is desirable. Furthermore, to capture epistemic
464 uncertainty of tsunami fragility models, multiple published models can be implemented using a
465 logic tree approach. However, such uncertainty modeling is not elaborated in this study.

466 Figure 8 shows comparisons of tsunami fragility curves by Suppasri et al. (2013a) for
467 different cases. As the damage states become severer, $\mu_{\ln IM|DS}$ and $\sigma_{\ln IM|DS}$ tend to become larger (i.e.
468 fragility curves shift towards the right and become flatter; Figure 8a). The *wash-away* fragility
469 curves for different materials are significantly different (Figure 8b), noting that the curves for wood
470 and all structures are similar due to the large proportion of wood structures in the MLIT database.
471 Figures 8c and 8d indicate that for RC and wood structures, the vulnerabilities for the 1-story and 2-
472 story are similar, whereas the vulnerability for the 3+-story is less. Thus distinction between low-
473 rise and mid/high-rise structures is an important consideration. The impact of adopting different
474 refinement levels of fragility curves on tsunami damage assessment is investigated in Section 3.2.

475 Finally, using the tsunami fragility curves, probabilities of attaining particular damage states
476 $p(DS=ds|im)$ can be estimated for each building and for each scenario (Figure 1 and Figure 8a). The
477 statistical analysis can be then carried out to develop site-specific tsunami risk curves and stochastic
478 tsunami risk maps. For instance, representative percentiles of $p(DS=ds)$ (e.g. median, 84th-
479 percentile, and 97.5-th percentile) can be displayed on a map to show the relative likelihood of
480 tsunami damage occurrence at different spatial scales (e.g. municipality versus regional levels).
481 Alternatively, cumulative distribution functions of $p(DS=ds|im)$ due to considered tsunami scenarios
482 can be assessed for individual buildings for comparison. Moreover, calculated values of $p(DS=ds)$
483 can be used in Monte Carlo sampling to generate realizations of individual damage states for the
484 buildings of interest. For instance, when the estimated *wash-away* damage probability of a RC
485 building is 0.2, a uniform random number between 0 and 1 can be generated; if the generated
486 random number is less than 0.2, the RC building is considered as washed out. The procedure can be
487 applied to all buildings within a city/town or region of interest. This resampling facilitates the

488 development of the cumulative distribution functions of the number of buildings having specific
489 damage states (which may be regarded as more practical metrics for tsunami risk management
490 purposes). By incorporating damage cost models for different buildings, the tsunami damage
491 assessment framework presented in Figure 1 can be further extended to carry out quantitative
492 tsunami loss estimation.
493
494 **3. Application**
495 Probabilistic tsunami damage assessment is performed for the pre-2011 building stock in the
496 Tohoku region. The main objective of this investigation is to assess the effects of variable tsunami
497 scenarios on the tsunami risk potential at municipality as well as regional levels using the developed
498 probabilistic tsunami risk analysis framework (Section 2).
499
500 **3.1 Problem set-up**
501 The building data that are considered in this study are obtained from the MLIT tsunami
502 damage database. The building data with the material type information and the story number less
503 than three stories are considered. The target buildings are located between Miyako and Soma
504 (Figure 6). The total number of the buildings is 124,735, consisting of 2277 RC structures, 7094
505 steel structures, 104,519 wood structures, and 10,845 masonry structures. 50,447 and 74,288
506 structures are 1-story and 2-story, respectively. Approximately, 40% of the buildings are located
507 along the Sanriku ria coast (Onagawa to Miyako), while the rest of 60% are located in the Sendai
508 coastal plain (Soma to Ishinomaki). It is noted that the considered building dataset covers the
509 majority of the low-rise buildings in the Tohoku region (with known material types) that were
510 exposed to tsunami inundation hazards, because the MLIT database includes all surveyed structures
511 with *no/minor damage*, which are located farther from the shore and at higher elevation.

512 The 726 source models that are generated by considering the eleven reference models and by
513 varying their source characteristics (i.e. geometry and slip distribution; 66 cases per reference
514 model) are adopted as a representative set (Section 2.2). In other words, the analysis results
515 presented in the following are dependent on this set-up. Alternatively, a different set of source
516 models may be adopted. Because the choice of the reference source models has major influence on
517 the tsunami simulation (Goda et al., 2014, 2015), results based on the Satake et al. source model
518 (out of 66 scenarios) are discussed in Section 3.2, and then in Section 3.3, results based on all 726
519 scenarios are discussed. The tsunami fragility assessment is carried out using the level-1 to level-3
520 tsunami fragility curves by Suppasri et al. (2013a). For the base case, the most refined level-3
521 fragility models are considered.

522 In the following, three representative cities and towns, i.e. Kamaishi, Onagawa, and Natori, as
523 well as the Tohoku region (Figure 6) are focused upon for the tsunami damage assessment. The
524 selection is to account for different terrain characteristics as well as for different tsunami wave
525 propagation paths, with the minimum number of locations. The drawn conclusions are applicable to
526 other locations, as long as local geographical features and relative positions to the asperities are
527 taken into account.

528

529 **3.2 Tsunami damage assessment using a single reference source model**

530 The source model by Satake et al. (2013) was developed by inverting eleven ocean-bottom
531 pressure gauge measurements, ten off-shore GPS wave gauge data, and 32 tidal wave gauge data
532 along the coastline. As the tsunami data were directly used in inversion analysis, the tsunami
533 simulation results based on the Satake et al. model are generally consistent with the observed off-
534 shore tsunami wave profiles and inundation data (Goda et al., 2014, 2015; see Figure 7). The
535 consideration of the source models based on Satake et al. (2013) serves as a benchmark for the
536 tsunami damage assessment based on a single reference source model.

Figure 9 and Figure 10 show the stochastic inundation depth maps and the *wash-away* damage probability maps for buildings located in Kamaishi, Onagawa, and Natori, respectively. Three percentile levels, i.e. 10^{th}, 50^{th} (median), and 90^{th}, are selected for illustration (note: they are to display both central and extreme cases; other percentiles can be adopted). These maps are developed by first evaluating the inundation depths for the 66 source models based on Satake et al. (2013) and then by calculating the corresponding *wash-away* damage probabilities using the fragility curves at individual building sites (note: other damage states can be considered but not shown in the figures). Subsequently, the statistics of the hazard/risk metrics at the chosen percentile levels are evaluated for each building, and finally, these statistics are displayed on the maps. Figure 9 captures the variability of inundation depth at the municipality level due to different tsunami scenarios, whereas Figure 10 displays the tsunami risk information by taking into account the structural vulnerability for variable tsunami hazard potential at building sites. The ranges of the hazard and risk maps shown in Figures 9 and 10 provide valuable information for tsunami evacuation and risk mitigation purposes in the future. For instance, in Onagawa, both spatial extent and severity of the tsunami hazard/risk increase as the percentile level increases. On the other hand, in Natori, spatial coverage of the affected buildings does not change significantly, when the inundation depth or damage potential becomes severer. The changing hazard and risk profiles for different scenarios depend on the local topography and bathymetry (flat versus steep terrains) as well as the proximity to large asperities. A major advantage of the stochastic risk maps (Figure 10) over the stochastic hazard maps (Figure 9) is that the impact of the increased tsunami hazard on the building stock in local communities is reflected. For example, the consequences due to the expanded 2-m deep inundated areas depend critically upon local building portfolios and their tsunami resistance (Figure 8b), which is highly nonlinear. This is the main motivation to promote the risk-based tsunami impact maps for coastal cities and towns.

561 The developed tsunami risk assessment framework can be further utilized to develop the
562 cumulative distribution function of tsunami risk metrics (i.e. tsunami risk curve), such as the
563 number of buildings that attain specific damage states. Given damage probabilities for all buildings,
564 damage states can be resampled by generating uniform random numbers and by comparing them
565 with damage probabilities for different damage states. In this study, the number of resampling is set
566 to 100 per building and tsunami source scenario (which is sufficient to obtain the stable results).
567 The results from this resampling are particularly useful for combining/aggregating the tsunami risk
568 impact for the building portfolios having different tsunami capacities (i.e. material type and story
569 number) at both local and regional levels. The aggregated tsunami risk curve retains the spatial
570 dependence of the tsunami hazard parameters for individual scenarios and is thus suitable for
571 assessing regional tsunami risk quantitatively. It is also noteworthy that the resampling can be
572 viewed as a simplified version of probabilistic tsunami loss estimation. By implementing
573 probabilistic cost models for the buildings, tsunami loss curves, rather than the cumulative
574 distribution functions of the number of buildings in specific damage states, can be obtained and
575 used for tsunami risk management.

576 Figure 11 shows the cumulative distribution functions of the number of buildings in the *wash-*
577 *away* damage state based on the Satake et al. source model for Kamaishi, Onagawa, Natori, and all
578 Tohoku region. For each location, four curves corresponding to different material types are included.
579 The horizontal axis of the figure is the damage ratio in terms of the number of buildings in the
580 *wash-away* damage state, normalized by the total number of buildings that are located within the
581 considered city/town or region. The vertical axis corresponds to the cumulative probability that is
582 defined based on 66 simulation cases (i.e. a single reference source model); for instance, a damage
583 ratio of 0.6 that corresponds to a probability level of 0.9 means that 90% of the 66 simulation cases
584 lead to damage ratios less than 0.6; in other words, only 10% of the simulated cases exceed the
585 damage ratio of 0.6. The total number of buildings in the designated areas is indicated inside the

586 brackets of the figure legend. Moreover, markers shown in the figure represent the actual damage
587 observed during the 2011 Tohoku Tsunami based on the MLIT database. For example, in Kamaishi,
588 there are 4,599 wood buildings; the simulated tsunami damage results for the *wash-away* damage
589 state vary widely for the damage ratio from 0.0 to 0.712 (= 3,275 buildings), depending on the
590 source models, whereas 3,300 buildings were washed away during the 2011 event (i.e. damage ratio
591 of 0.718; green triangle marker). The probability levels that correspond to the observed damage
592 ratios for different material types can be different in a given city/town; for instance, in Kamaishi
593 (Figure 11a), the probability level for RC buildings is about 0.6, whereas those for
594 steel/wood/masonry buildings exceed 0.8. Such differences are caused by two factors. The first is
595 the different spatial distribution of buildings for each material type (i.e. prediction accuracy at
596 building locations varies spatially). The second is the difference between the actual damage
597 observations and the adopted fragility models. The model bias of tsunami fragility curves is present
598 because the fragility models by Suppasri et al. (2013) are developed at regional level, rather than
599 municipality level.

600 Various useful insights can be gained from the results shown in Figure 11. Comparison of the
601 cumulative distribution functions for different material types and for different locations indicates
602 the variability of the tsunami risk is affected by various factors. The curves for wood and masonry
603 buildings vary more widely than those for RC and steel buildings and are located towards the right-
604 hand side of the figure (i.e. reaching higher damage ratios at the same probability levels), reflecting
605 the differences of the tsunami vulnerability for these material types (Figure 8b). In Kamaishi and
606 Onagawa, the risk curves for wood and masonry are similar, while they are different in Natori (and
607 the Tohoku region). The observed difference of the risk curves for wood and masonry buildings in
608 Natori can be explained by the fact that the tsunami inundation depth in Natori is not as high as in
609 Kamaishi and Onagawa (see Figure 9) and the inundation depth in Natori is sufficient to cause the
610 *wash-away* damage for the majority of wood buildings in Natori but not for the majority of masonry

611 buildings in Natori (note: up to about 60% of the masonry buildings may be washed out, but not up
612 to 80%). The probability levels corresponding to the observed damage during the 2011 event (see
613 the markers shown in Figure 11) provide retrospective indications regarding how rare/extreme the
614 2011 Tohoku Tsunami damage was in terms of the simulated tsunami risk curves (i.e. anticipated
615 tsunami risk for M_w9 earthquakes). For instance, the observed damage in Kamaishi and Onagawa
616 (except for RC buildings) corresponds to relatively high risk (i.e. probability) levels, while that in
617 Natori is relatively low; the overall risk level of the actual damage for the Tohoku region is
618 relatively high, indicating that the observed tsunami damage is severer than the expected tsunami
619 risk level for the considered scenarios. Note that such interpretations should be specific to the
620 considered tsunami scenarios (and underlying assumptions). One particular source model by Satake
621 et al. is focused upon herein; the evaluations of the observed tsunami with regard to the simulation
622 results are revisited in Section 3.3 by considering multiple reference source models.

623 Figure 12 presents two sets of cumulative distribution functions of the number of buildings
624 based on the Satake et al. source model for Kamaishi, Onagawa, Natori, and the Tohoku region: one
625 is for the *wash-away* damage state (thin lines) and the other is for the exceedance of the *complete*
626 *damage* state (i.e. including the damage cases for *wash-way*, *collapse*, and *complete damage*; thick
627 lines). In this figure, to reduce the clutter, results for RC and wood buildings only are included. The
628 risk curves for the *complete* damage are positioned to the right-hand side of those for the *wash-*
629 *away* damage. The behavior and variability of the risk curves depend on the location, material type,
630 and damage state. It is also noted that the tsunami risk level for the observed damage is dependent
631 upon the damage state. A noticeable case is for RC buildings in Onagawa; when the *wash-away*
632 damage state is considered, the observed damage is not extreme with respect to a range of tsunami
633 risk predictions based on the simulation (i.e. even severer damage is possible), whereas when the
634 exceedance of *complete damage* is focused upon, the observed damage is an extreme case.

635 Finally, the impact of adopting different refinement levels of fragility curves on tsunami
636 damage assessment is investigated. Figure 13 compares the cumulative distribution functions of the
637 number of buildings in the *wash-away* damage state based on the Satake et al. source model by
638 considering three refinement levels of the tsunami fragility models (Figures 8c and 8d). Results for
639 RC buildings in Kamaishi and for wood buildings in Natori are presented in Figure 13a and Figure
640 13b, respectively. The consideration of material-type-specific tsunami fragility curves has major
641 influence on the tsunami damage assessment for the RC buildings (Figure 13a); the substitution of
642 the fragility models for all data (which are dominated by numerous *wash-away* wood buildings)
643 results in significant overestimation (level-1 versus level-2 or level-3). Figure 13a also indicates that
644 the consideration of the story number in tsunami damage assessment of RC buildings may result in
645 noticeable differences of the tsunami risk curves. The differences of the tsunami risk curves for
646 wood buildings are generally much less noticeable than RC buildings, in particular, level-1 versus
647 level-2 or level-3. This is simply because the *wash-away* fragility curves for all buildings and for
648 wood buildings are similar (Figure 8d). The distinction of the story number shows noticeable
649 differences of the risk curves. It is noteworthy that these differences of the risk curves are highly
650 dependent on the locations or more specifically the tsunami inundation depth. When wood buildings
651 are subjected to 10-m deep inundation, the differences in fragility curves do not make much
652 difference in terms of risk curves. The results suggest that using the accurate and reliable tsunami
653 fragility models is important, and care must be taken to avoid significant bias in the tsunami
654 damage assessment.
655
656 **3.3 Tsunami damage assessment using multiple reference source models**
657 The model uncertainty of the tsunami source characteristics has significant impact on the
658 predicted tsunami hazards (Goda et al., 2014, 2015), and thus on the tsunami risk and damage

659 metrics. The main focus of this section is to evaluate such impact by considering multiple reference
660 source models.

661 Figure 14 and Figure 15 show the comparison of cumulative distribution functions of the
662 number of RC buildings and wood buildings, respectively, in the *wash-away* damage state based on
663 the eleven source models for Kamaishi, Onagawa, Natori, and the Tohoku region. In the figures,
664 separate curves are presented for individual reference source models (note: each curve is based on
665 66 source models). The visual inspections of Figures 14 and 15 clearly illustrate that the effects of
666 considering different reference source models are significant for both RC and wood buildings (also
667 applicable to steel and masonry buildings). The dependency on different source models varies with
668 locations and material types (and damage states, though not presented). By focusing upon the
669 variability of the damage ratio for the RC buildings at the probability level of 0.5 (Figure 14), the
670 ranges of the damage ratios for the eleven reference models are between 0.1 and 0.4 for Kamaishi,
671 Onagawa, and Natori, while those for the entire Tohoku region is narrower (between 0.1 and 0.25).
672 The corresponding variability of the median damage ratio for wood buildings is greater than that for
673 RC buildings (i.e. Figure 14 versus Figure 15); the ranges are between 0.3 and 0.8 for Kamaishi,
674 Ongawa, and Natori, and are between 0.15 and 0.40 for the Tohoku region. Especially, the tsunami
675 risk curves for wood buildings in Natori (among the cases presented in Figures 14 and 15) vary
676 significantly; the risk curves for models 9 to 11 exhibit different distribution behavior of the
677 tsunami damage characteristics in comparison with other models. These differences reflect the
678 complex nonlinear relationship between the tsunami sources and the tsunami risk metrics, affected
679 by the terrain features, relative positions of the site and the asperities, and building stock (i.e.
680 tsunami fragility). It is important to point out that the relative tsunami risk (i.e. probability) levels of
681 the observed damage during the 2011 Tohoku Tsunami in terms of the simulated damage results
682 vary widely, depending on the selected reference source models. The probabilities that correspond
683 to the observed tsunami damage for RC buildings range from 0.2 to 0.75 for Kamaishi, from 0.1 to

684 0.5 for Onagawa, from 0.0 to 0.2 for Natori, and from 0.2 to 1.0 for the Tohoku region, respectively
685 (Figure 14). The counterparts for wood buildings are from 0.75 to 1.0 for Kamaishi, from 0.95 to
686 1.0 for Onagawa, from 0.0 to 0.75 for Natori, and from 0.5 to 1.0 for the Tohoku region,
687 respectively (Figure 15). In light of wide variations of the tsunami risk levels of the observed
688 damage during the 2011 Tohoku Tsunami relative to the simulation results, for some cases, it may
689 be difficult to conclude that the 2011 Tohoku Tsunami damage was a worst-case scenario. The
690 implication of the results is that the local and regional evacuation scenarios may not be developed
691 by simply assuming that the Tohoku Tsunami was an extraordinary situation and thus cannot be
692 adopted as the critical scenario for all locations along the Tohoku coast uniformly. Rather, a wide
693 range of tsunami scenarios should be developed based on the up-to-date seismological knowledge
694 as well as geophysical observations, and evaluated to identify the critical scenarios for tsunami
695 evacuation and risk mitigation (as was done in this study).

696 Figure 16 shows the cumulative distribution functions of the number of buildings in the *wash-*
697 *away* damage state based on the eleven source models for Kamaishi, Onagawa, Natori, and the
698 Tohoku region. The tsunami risk curves are integrated for all reference source models (i.e. 726
699 cases). The effects of taking into account the multiple reference source models with respect to the
700 results based on a single reference source model (e.g. Satake et al. model) can be investigated by
701 comparing Figure 11 and Figure 16. The consideration of multiple reference models results in a
702 wider variation of the risk curves; differences are more noticeable at low and high probability levels.
703 As long as the reference source models that are adopted in Monte Carlo tsunami simulation are
704 deemed as reasonable representation of the future critical scenarios for tsunami emergency
705 preparedness, inclusion of more extreme cases provides tsunami experts, policy makers, emergency
706 officers, and local residents with useful information related to the uncertainties associated with
707 tsunami hazard/risk predictions. An open communication among the stakeholders is the key to
708 improve the resilience of local coastal communities against catastrophic tsunami events.

4. Conclusions

Tsunami inundation is a highly nonlinear process and causes catastrophic damage to buildings and infrastructure in coastal cities and towns. The spatial as well as depth extent of the tsunami inundation is greatly influenced by the tsunami source characteristics. Consequently, the uncertainty associated with tsunami sources has major impact on the tsunami risk and damage. To account for the propagating effects of tsunami source uncertainty in tsunami damage assessment, a probabilistic framework for tsunami risk analysis was developed using Monte Carlo tsunami simulation (without relying on an artificial scenario-based approach), taking into account variable source geometry and stochastic slip distribution, together with tsunami fragility models for different building types. The developed analytical tool was applied to actual building stock in the Tohoku region, Japan, subject to M_w9-class mega-thrust subduction earthquakes. The innovative aspects of the developed computational tool and framework were that variable tsunami source models were generated based on the spectral analysis and synthesis method by considering multiple reference source models (i.e. epistemic uncertainty), and that the uncertainty associated with tsunami source characteristics was propagated consistently to evaluate the tsunami risk curves for the building portfolio. The cumulative distribution functions of the number of buildings in different damage states were compared to investigate the variability of the tsunami risk curves due to tsunami source characteristics, terrain features, and structural/material characteristics. The simulation results were also compared with the actual tsunami damage observations during the 2011 Tohoku event. The extended assessment of the sensitivity and variability of the tsunami risk metrics, rather than tsunami hazard parameters, provides tsunami analysts and local stakeholders with valuable information for improved tsunami risk management and risk/uncertainty communication.

The main conclusions of this study are:

- The stochastic tsunami risk maps depend on the local topography (flat versus steep terrains), the proximity to large asperities, and local building portfolios. Risk-based tsunami impact

maps for coastal cities and towns have advantages over stochastic inundation depth maps because the potential consequences due to the anticipated tsunami hazards on the building stock are incorporated.

- Tsunami risk curves are affected by structural material types, locations, and considered damage states for the adopted tsunami metrics. In addition, refinement levels of tsunami fragility curves (i.e. material type and story number) can have major influence on the tsunami damage assessment. The interacting effects of these key risk factors and model components are complex.
- The effects of considering different reference source models on tsunami risk curves are significant for all material types, locations, and damage states. They reflect the complex nonlinear relationship between the tsunami sources and the tsunami risk metrics.
- The tsunami risk (probability) levels corresponding to the observed damage during the 2011 event provide useful retrospective indications regarding how rare/extreme the 2011 Tohoku Tsunami damage was in terms of the simulated tsunami risk curves. However, such observations depend on the selected reference source models. Therefore, in determining critical scenarios for tsunami evacuation and risk mitigation at local as well as regional levels, a wide range of possible tsunami scenarios should be considered in light of the current seismological knowledge and geophysical observations.

As a final remark, in light of deep epistemic uncertainty (Kagan and Jackson, 2013; Stein and Stein, 2013), stochastic source models that are considered in this study may not be representative for future events and may not capture extremely rare cases. Furthermore, variations of magnitude ranges for a given tsunami source and land surface roughness give additional uncertainty of probabilistic tsunami characteristics. The potential limitation of the proposed method should be kept in mind by tsunami analysts and should be communicated with decision makers and stakeholders.

These issues become critical when the stochastic method is applied to future tsunami hazard predictions without empirical constraints.

Acknowledgments

The bathymetry and elevation data for the Tohoku region were provided by the Cabinet Office of the Japanese Government. The run-up and inundation survey data were obtained from the 2011 Tohoku Earthquake Tsunami Joint Survey Group (http://www.coastal.jp/tsunami2011/). The tsunami damage data for the 2011 Tohoku earthquake were obtained from the Ministry of Land, Infrastructure, and Transportation (http://www.mlit.go.jp/toshi/toshi-hukkou-arkaibu.html). This work was supported by the Engineering and Physical Sciences Research Council (EP/M001067/1).

References

Ammon, C.J., Lay, T., Kanamori, H., and Cleveland, M. (2011). A rupture model of the 2011 off the Pacific coast of Tohoku earthquake. Earth Planets Space 63, 693–696.

Borrero, J. (2005). Field survey of northern Sumatra and Banda Aceh, Indonesia after the tsunami and earthquake of 26 December 2004. Seismol. Res. Lett. 76, 309–318.

Bunya, S., Deitrich, J.C., Westerink, J.J., Ebersole, B.A., Smith, J.M., Atkinson, J.H., Jensen, R., REsio, D.T., Luettich, R.A., Dawson, C., Cardone, V.J., Cox, A.T., Powell, M.D., Westerink, H.J., and Roberts, H.J. (2010). A high-resolution coupled riverine flow, tide, wind, wind wave, and storm surge model for southern Louisiana and Mississippi. part I: model development and validation. Mon. Wea. Rev., 18, 345–377.

Charvet, I., Ioannou, I., Rossetto, T., Suppasri, A., and Imamura, F. (2014). Empirical fragility assessment of buildings affected by the 2011 Great East Japan tsunami using improved statistical models. Nat. Haz. 73, 951–973.

782 Federal Emergency Management Agency (FEMA) (2008). Guidelines for design of structures for
783 vertical evacuation from tsunamis. FEMA P646, Washington DC.
784 Fraser, S., Pomonis, A., Raby, A., Goda, K., Chian, S.C., Macabuag, J., Offord, M., Saito, K., and
785 Sammonds, P. (2013). Tsunami damage to coastal defences and buildings in the March 11th
786 2011 M_w9.0 Great East Japan earthquake and tsunami. Bull. Earthq. Eng. 11, 205–239.
787 Fraser, S., Power, W.L., Wang, X., Wallace, L.M., Mueller, C., and Johnston, D.M. (2014).
788 Tsunami inundation in Napier, New Zealand, due to local earthquake sources. Nat. Haz. 70,
789 415–445.
790 Fujii, Y., Satake, K., Sakai, S., Shinohara, S., and Kanazawa, T. (2011). Tsunami source of the
791 2011 off the Pacific coast of Tohoku earthquake. Earth Planets Space 63, 815–820.
792 Fukutani, Y., Suppasri, A., and Imamura, F. (2015). Stochastic analysis and uncertainty assessment
793 of tsunami wave height using a random source parameter model that targets a Tohoku-type
794 earthquake fault. Stoch. Environ. Res. Risk Assess., doi: 10.1007/s00477-014-0966-4.
795 Geist, E.L. (2002). Complex earthquake rupture and local tsunamis. J. Geophys. Res. Solid Earth,
796 doi:10.1029/2000JB000139.
797 Geist, E.L., and Parsons, T. (2006). Probabilistic analysis of tsunami hazards. Nat. Haz. 37, 277–
798 314.
799 Goda, K., Mai, P.M., Yasuda, T., and Mori, N. (2014). Sensitivity of tsunami wave profiles and
800 inundation simulations to earthquake slip and fault geometry for the 2011 Tohoku earthquake.
801 Earth Planets Space 66, 105, doi:10.1186/1880-5981-66-105.
802 Goda, K., Yasuda, T., Mori, N., and Mai, P.M. (2015). Variability of tsunami inundation footprints
803 considering stochastic scenarios based on a single rupture model: application to the 2011
804 Tohoku earthquake. J. Geophys. Res. Oceans, doi:10.1002/2014JC010626.

805 Goto, C., Ogawa, Y., Shuto, N., and Imamura, F. (1997). Numerical method of tsunami simulation
806 with the leap-frog scheme (IUGG/IOC Time Project). IOC Manual, UNESCO, No. 35, Paris,
807 France.
808 Gusman, A.R., Tanioka, Y., Sakai, S., and Tsushima, H. (2012). Source model of the great 2011
809 Tohoku earthquake estimated from tsunami waveforms and crustal deformation data. Earth
810 Planet Sci. Lett. 341–344, 234–242.
811 Hayes, G.P. (2011). Rapid source characterization of the 2011 M_w 9.0 off the Pacific coast of
812 Tohoku earthquake. Earth Planets Space 63, 529–634.
813 Horspool, N., Pranantyo, I., Griffin, J., Latief, H., Natawidjaja, D.H., Kongko, W., Cipta, A.,
814 Bustaman, B., Anugrah, S.D., and Thio, H.K. (2014). A probabilistic tsunami hazard
815 assessment for Indonesia. Nat. Haz. Earth Syst. Sci. 14, 3105–3122.
816 Iinuma, T., Ohzono, M., Ohta, Y., and Miura, S. (2011). Coseismic slip distribution of the 2011 off
817 the Pacific coast of Tohoku earthquake (M9.0) estimated based on GPS data – was the
818 asperity in Miyagi-oki ruptured? Earth Planets Space 63, 643–648.
819 Iinuma, T., Hino, R., Kido, M., Inazu, D., Osada, Y., Ito, Y., Ohzono, M., Tsushima, H., Suzuki, S.,
820 Fujimoto, H., and Miura, S. (2012). Coseismic slip distribution of the 2011 off the Pacific
821 coast of Tohoku earthquake (M9.0) refined by means of seafloor geodetic data. J. Geophys.
822 Res. Solid Earth, doi:10.1029/2012JB009186.
823 Kagan, Y., and Jackson, D.D. (2013). Tohoku earthquake: a surprise? Bull. Seismol. Soc. Am. 103,
824 1181–1194.
825 Kaiser, G., Scheele, L., Kortenhaus, A., Løvholt, F., Römer, H., and Leschka, S. (2011). The
826 influence of land cover roughness on the results of high resolution tsunami inundation
827 modeling. Nat. Haz. Earth Syst. Sci. 11, 2521–2540.

828 Koshimura, S., Oie, T., Yanagisawa, H., and Imamura, F. (2009). Developing fragility functions for
829 tsunami damage estimation using numerical model and post-tsunami data from Banda Aceh,
830 Indonesia. Coast. Eng. J. 51, 243–273, doi:10.1142/S0578563409002004.
831 Lavallée, D., Liu, P., and Archuleta, R.J. (2006). Stochastic model of heterogeneity in earthquake
832 slip spatial distributions. Geophys. J. Int. 165, 622–640.
833 Løvholt, F., Pedersen, G., Bazin, S., Kuhn, D., Bredesen, R.E., and Harbitz, C. (2012). Stochastic
834 analysis of tsunami runup due to heterogeneous coseismic slip and dispersion. J. Geophys.
835 Res. Oceans, doi:10.1029/2011JC007616.
836 Mai, P.M., and Beroza, G.C. (2002). A spatial random field model to characterize complexity in
837 earthquake slip. J. Geophys. Res. Solid Earth, doi:10.1029/2001JB000588.
838 Mai, P.M., Spudich, P., and Boatwright, J. (2005). Hypocenter locations in finite-source rupture
839 models. Bull. Seismol. Soc. Am. 95, 965–980.
840 Mas, E., Koshimura, S., Suppasri, A., Matsuoka, M., Matsuyamaa, M., Yoshii, T., Jimenez, C.,
841 Yamazaki, F., and Imamura, F. (2012). Developing tsunami fragility curves using remote
842 sensing and survey data of the 2010 Chilean tsunami in Dichato. Nat. Haz. Earth Syst. Sci. 12,
843 2689–2697.
844 McCloskey, J., Antonioli, A., Piatanesi, A., Sieh, K., Steacy, S., Nalbant, S., Cocco, M., Giunchi,
845 C., Huang, J.D., and Dunlop, P. (2008). Tsunami threat in the Indian Ocean from a future
846 megathrust earthquake west of Sumatra. Earth Planet Sci. Lett. 265, 61–81.
847 McGuire, R.K. (2004). Seismic hazard and risk analysis. Earthquake Eng. Res. Institute, Oakland,
848 CA, USA.
849 Ministry of Land, Infrastructure, and Transportation (MLIT) (2014). Survey of tsunami damage
850 condition. http://www.mlit.go.jp/toshi/toshi-hukkou-arkaibu.html. Accessed 1 July 2014.
851 Mori, N., Takahashi, T., Yasuda, T., Yanagisawa, H. (2011). Survey of 2011 Tohoku earthquake
852 tsunami inundation and run-up. Geophys. Res. Lett., doi:10.1029/2011GL049210.

853 Mueller, C., Power, W., Fraser, S., and Wang, X. (2015). Effects of rupture complexity on local
854 tsunami inundation: Implications for probabilistic tsunami hazard assessment by example. J.
855 Geophys. Res. Solid Earth 120, doi:10.1002/2014JB011301.
856 Murata, S., Imamura, F., Katoh, K., Kawata, Y., Takahashi, S., and Takayama, T. (2010). Tsunami:
857 to survive from tsunami. World Scientific Publishing, Hackensack, NJ, USA.
858 Okada, Y. (1985). Surface deformation due to shear and tensile faults in a half-space. Bull. Seismol.
859 Soc. Am. 75, 1135–1154.
860 Pang, A. (2008). Visualizing uncertainty in natural hazards. Risk Gov. Soc. 14, 261–294.
861 Reese, S., Bradley, B.A., Bind, J., Smart, G., Power, W., and Sturman, J. (2011). Empirical building
862 fragilities from observed damage in the 2009 South Pacific tsunami. Earth Sci. Rev. 107,
863 156–173.
864 Satake, K., Fujii, Y., Harada, T., and Namegaya, Y. (2013). Time and space distribution of
865 coseismic slip of the 2011 Tohoku earthquake as inferred from tsunami waveform data. Bull.
866 Seismol. Soc. Am. 103, 1473–1492.
867 Shao, G., Li, X., Ji, C., and Maeda, T. (2011). Focal mechanism and slip history of the 2011 M_w 9.1
868 off the Pacific coast of Tohoku earthquake, constrained with teleseismic body and surface
869 waves. Earth Planet Space 63, 559–564.
870 Stein, S., and Stein, J.L. (2013). Shallow versus deep uncertainties in natural hazard assessments.
871 EOS 94, 133–134.
872 Suppasri, A., Imamura, F., and Koshimura, S. (2010). Effect of the rupture velocity of fault motion,
873 ocean current and initial sea level on the transoceanic propagation of tsunami. Coast. Eng. J.
874 52, 107–132.
875 Suppasri, A., Koshimura, S., and Imamura, F. (2011). Developing tsunami fragility curves based on
876 the satellite remote sensing and the numerical modeling of the 2004 Indian Ocean tsunami in
877 Thailand. Nat. Haz. Earth Syst. Sci. 11, 173–189.

878 Suppasri, A., Mas, E., Charvet, I., Gunasekera, R., Imai, K., Fukutani, Y., Abe, Y., and Imamura, F.
879 (2013a). Building damage characteristics based on surveyed data and fragility curves of the
880 2011 Great East Japan tsunami. Nat. Haz. 66, 319–341.
881 Suppasri, A., Shuto, N., Imamura, F., Koshimura, S., Mas, E., and Yalciner, A.C. (2013b). Lessons
882 learned from the 2011 Great East Japan tsunami: performance of tsunami countermeasures,
883 coastal buildings, and tsunami evacuation in Japan. Pure Appl. Geophys. 170, 993–1018.
884 Tanioka, Y., and Satake, K. (1996). Tsunami generation by horizontal displacement of ocean
885 bottom. Geophys. Res. Lett. 23, 861–864.
886 Tarbotton, C., Dall'Osso, F., Dominey-Howes, D., and Goff, J. (2015). The use of empirical
887 vulnerability functions to assess the response of buildings to tsunami impact: comparative
888 review and summary of best practice. Earth Sci. Rev. 142, 120–134.
889 Thio, H.K., Somerville, P., and Ichinose, G. (2007). Probabilistic analysis of strong ground motion
890 and tsunami hazards in southeast Asia. J. Earthq. Tsunami 1, 119–137.
891 Wiebe, D.M., and Cox, D.T. (2014). Application of fragility curves to estimate building damage
892 and economic loss at a community scale: a case study of Seaside, Oregon. Nat. Haz. 71,
893 2043–2061.
894 Yamazaki, Y., Lay, T., Cheung, K.F., Yue, H., and Kanamori, H. (2011). Modeling near-field
895 tsunami observations to improve finite-fault slip models for the 11 March 2011 Tohoku
896 earthquake. Geophys. Res. Lett., doi:10.1029/2011GL049130.
897 Yoshikawa, H., and Goda, K. (2014). Financial seismic risk analysis of building portfolios. Nat.
898 Haz. Rev. 15, 112–120.
899
900
901

Table 1. Summary of the eleven reference source models and the stochastic source parameters.

Model ID and reference	Reference source model parameters					Stochastic source model parameters			
	Moment magnitude	[Fault length, fault width] (km)	Top-edge depth (km)	[Strike, dip, rake] (°)	Data type	von Kármán parameters [A_z (km), A_x (km), H]	Box–Cox parameter	Asperity-zone dimension fraction[2] [down-dip, along-strike]	Asperity slip fraction[3]
1: Fujii et al. (2011)	9.02	[500, 200]	0.0	[193, 14, 81]	Tsunami	[63, 68, 0.99]	0.2	[0.35, 0.35]	0.4
2: Satake et al. (2013)	9.05	[550, 200]	0.0	[193, 8-16, 81]	Tsunami	[56, 107, 0.82]	0.2	[0.25, 0.4]	0.3
3: Shao et al. (2011) [Ver1]	9.13	[500, 200]	4.9	[198, 10, *Var*[1]]	Teleseismic	[50, 119, 0.99]	0.3	[0.25, 0.4]	0.35
4: Shao et al. (2011) [Ver2]	9.14	[475, 200]	7.4	[198, 10, *Var*]	Teleseismic	[53, 84, 0.99]	0.3	[0.3, 0.4]	0.35
5: Shao et al. (2011) [Ver3]	9.14	[475, 200]	7.4	[198, 10, *Var*]	Teleseismic	[45, 93, 0.99]	0.3	[0.3, 0.4]	0.35
6: Yamazaki et al. (2011)	8.97	[340, 200]	3.8	[192, 12, *Var*]	Teleseismic & tsunami	[37, 72, 0.96]	0.2	[0.3, 0.4]	0.4
7: Ammon et al. (2011)	9.00	[600, 210]	1.0	[202, 12, 85]	Teleseismic & geodetic	[51, 94, 0.99]	0.3	[0.4, 0.35]	0.3
8: Gusman et al. (2012)	9.11	[450, 200]	1.0	[202, 5-20, *Var*]	Tsunami & geodetic	[64, 86, 0.99]	0.2	[0.3, 0.35]	0.3
9: Hayes (2011)	9.09	[625, 260]	5.8	[194, 10, *Var*]	Teleseismic	[65, 94, 0.99]	0.2	[0.3, 0.4]	0.3
10: Iinuma et al. (2011)	9.03	[600, 240]	1.1	[*Var*, *Var*, *Var*]	Geodetic	[54, 141, 0.99]	0.1	[0.3, 0.3]	0.25
11: Iinuma et al. (2012)	9.03	[620, 260]	1.0	[*Var*, *Var*, *Var*]	Geodetic	[51, 81, 0.99]	0.0	[0.45, 0.3]	0.45

[1] *Var* represents that the parameter is variable; [2] The fraction values of the asperity rectangle for the down-dip and along-strike directions are defined in terms fault length and fault width of the original slip model; and [3] The fraction value of the asperity slip concentration is defined in terms of total slip over the fault plane.

906 **Figure Captions**

907 Figure 1. Framework for probabilistic tsunami hazard/risk analysis.

908 Figure 2. Stochastic source modeling: Step 1 – preliminary analysis.

909 Figure 3. Stochastic source modeling: Step 2 – spectral analysis.

910 Figure 4. Stochastic source modeling: Step 3 – spectral synthesis.

911 Figure 5. Eleven inversion-based source models. The sub-fault with thick lines represents the
912 asperity area, slip of which is equal to or greater than three times the average slip.

913 Figure 6. Maximum wave height contour map based on the source model by Satake et al. (2013)
914 and locations of coastal cities and towns in the Tohoku region.

915 Figure 7. Comparison of tsunami simulation results based on the source model by Satake et al.
916 (2013) with the Tohoku Tsunami Joint Survey (TTJS) data (Mori et al., 2011) in
917 Kamaishi, Onagawa, and Sendai-Natori-Iwanuma: (a) inundation depth contours and (b)
918 scatter plot.

919 Figure 8. Empirical tsunami fragility curves based on the 2011 Tohoku Tsunami damage data
920 (Suppasri et al., 2013a).

921 Figure 9. Stochastic inundation depth maps at the 10th, 50th, and 90th percentiles based on the
922 Satake et al. source model: (a) Kamaishi, (b) Onagawa, and (c) Natori.

923 Figure 10. Stochastic *wash-away* damage probability maps at the 10th, 50th, and 90th percentiles
924 based on the Satake et al. source model: (a) Kamaishi, (b) Onagawa, and (c) Natori.

925 Figure 11. Cumulative distribution functions of the number of buildings in the *wash-away* damage
926 state based on the Satake et al. source model: (a) Kamaishi, (b) Onagawa, (c) Natori,
927 and (d) all cities and towns in the Tohoku region.

928 Figure 12. Comparison of cumulative distribution functions of the number of RC/wood buildings
929 in the *wash-away* and *complete damage* states based on the Satake et al. source model:
930 (a) Kamaishi, (b) Onagawa, (c) Natori, and (d) all cities and towns in the Tohoku region.

931 Figure 13. Cumulative distribution functions of the number of buildings in the *wash-away* damage
932 state based on the Satake et al. source model by considering different refinement levels
933 of tsunami fragility models: (a) RC buildings in Kamaishi and (b) wood buildings in
934 Natori.
935 Figure 14. Cumulative distribution functions of the number of RC buildings in the *wash-away*
936 damage state based on the eleven source models (separate curves for individual
937 reference source models): (a) Kamaishi, (b) Onagawa, (c) Natori, and (d) all cities and
938 towns in the Tohoku region.
939 Figure 15. Cumulative distribution functions of the number of wood buildings in the *wash-away*
940 damage state based on the eleven source models (separate curves for individual
941 reference source models): (a) Kamaishi, (b) Onagawa, (c) Natori, and (d) all cities and
942 towns in the Tohoku region.
943 Figure 16. Cumulative distribution functions of the number of buildings in the *wash-away* damage
944 state based on the eleven source models (integrated curves for all reference source
945 models): (a) Kamaishi, (b) Onagawa, (c) Natori, and (d) all cities and towns in the
946 Tohoku region.

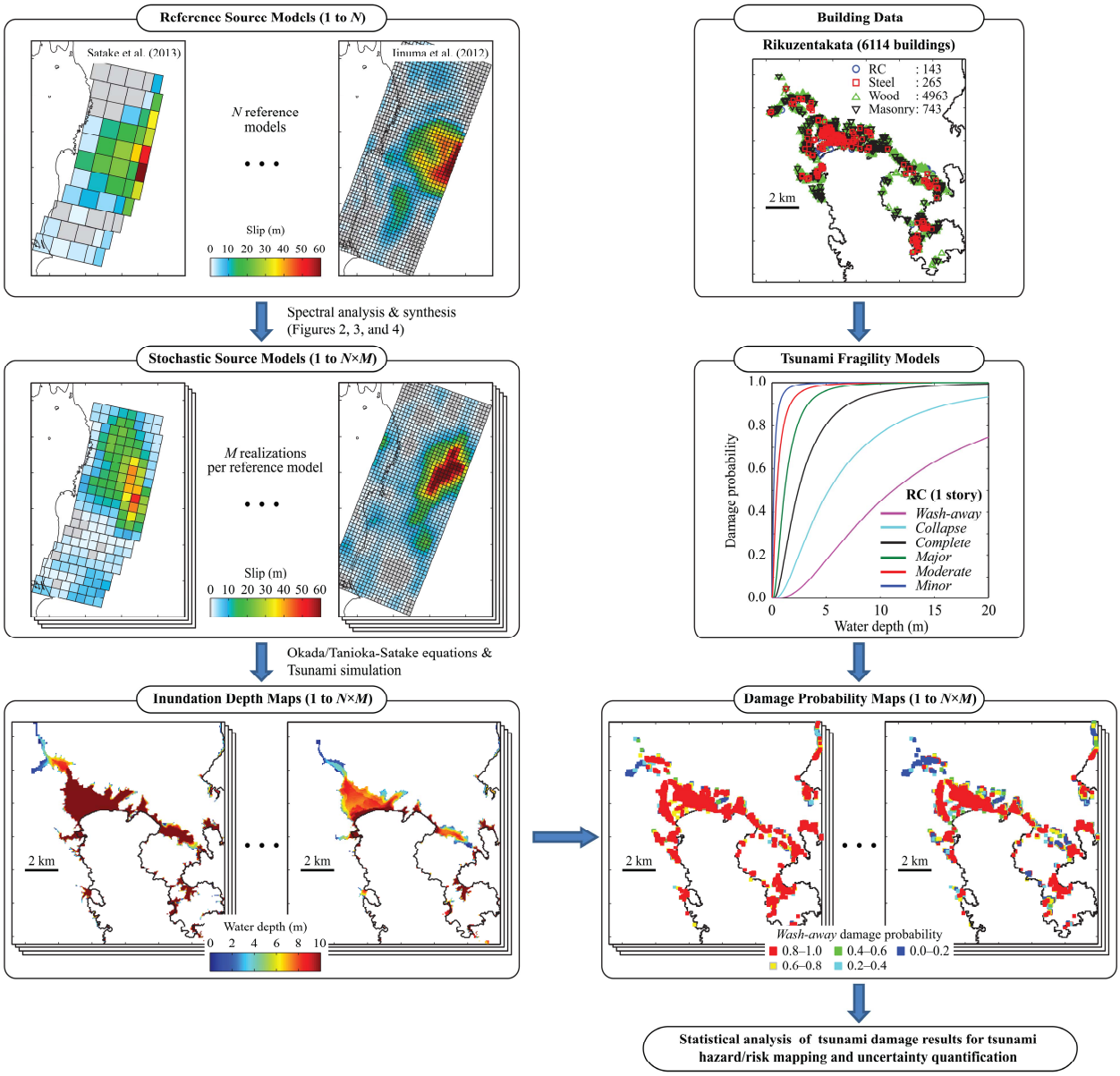

Figure 1. Framework for probabilistic tsunami hazard/risk analysis.

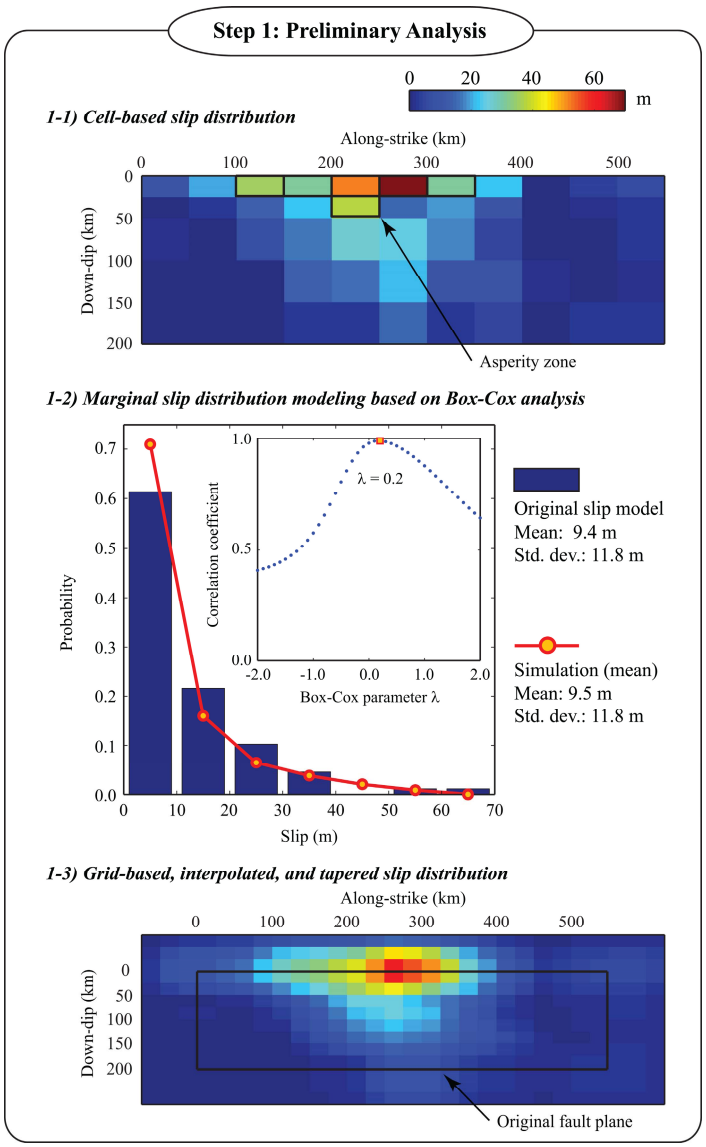

Figure 2. Stochastic source modeling: Step 1 – preliminary analysis.

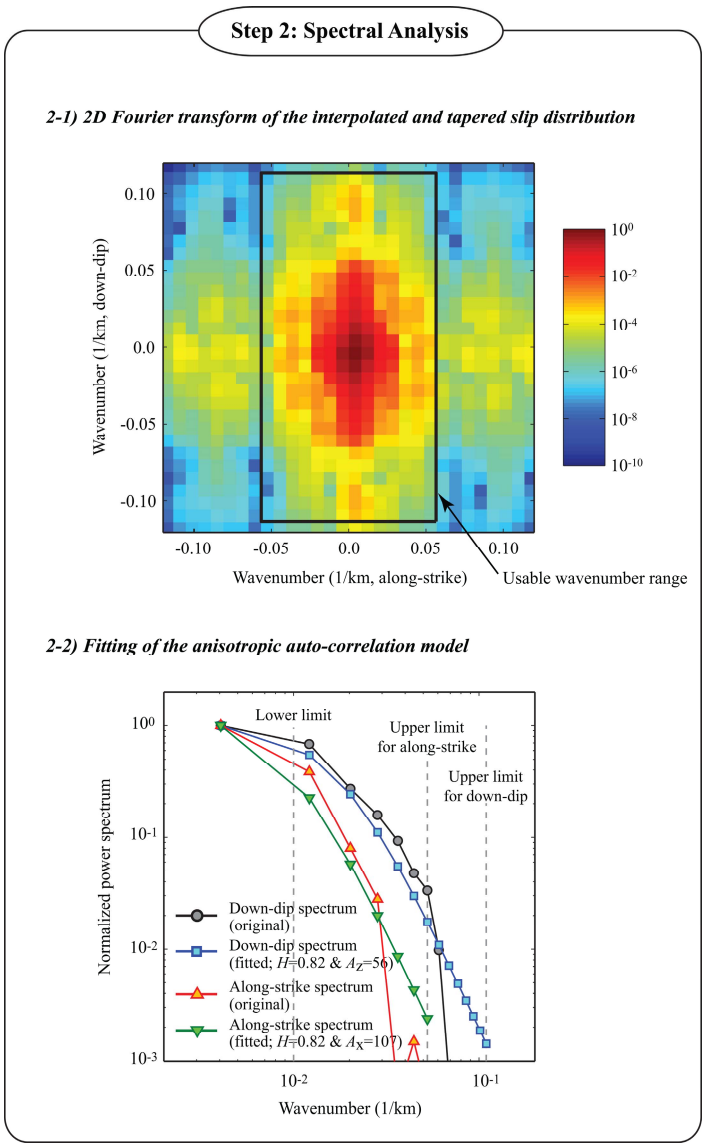

Figure 3. Stochastic source modeling: Step 2 – spectral analysis.

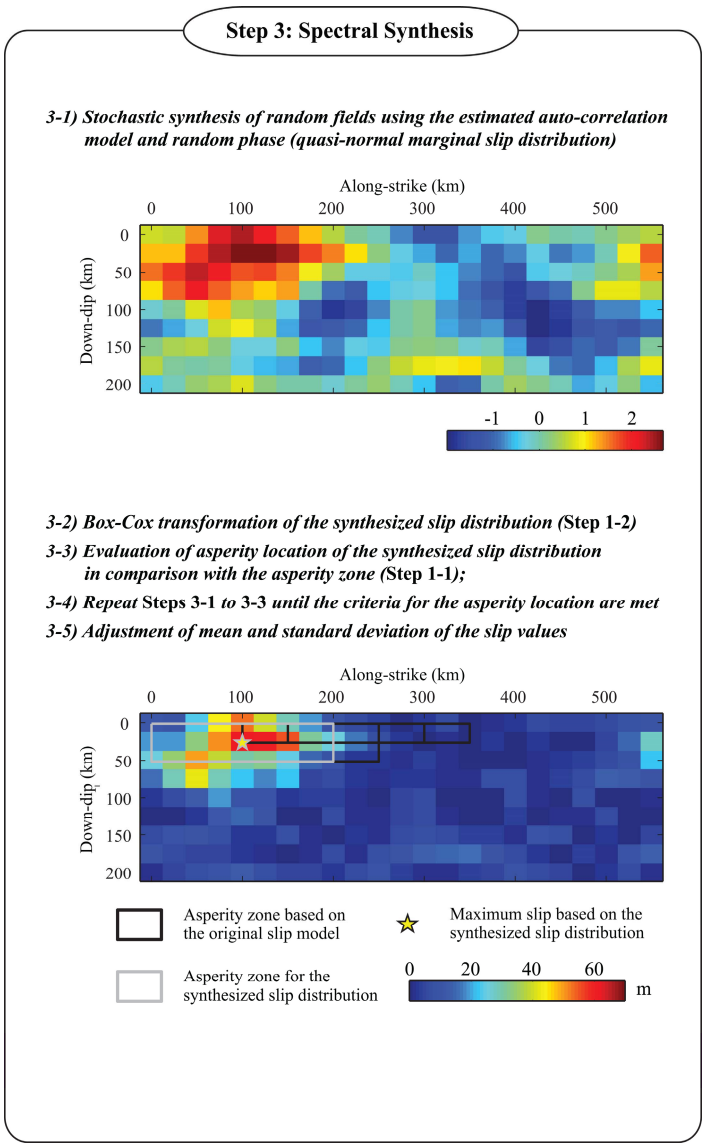

Figure 4. Stochastic source modeling: Step 3 – spectral synthesis.

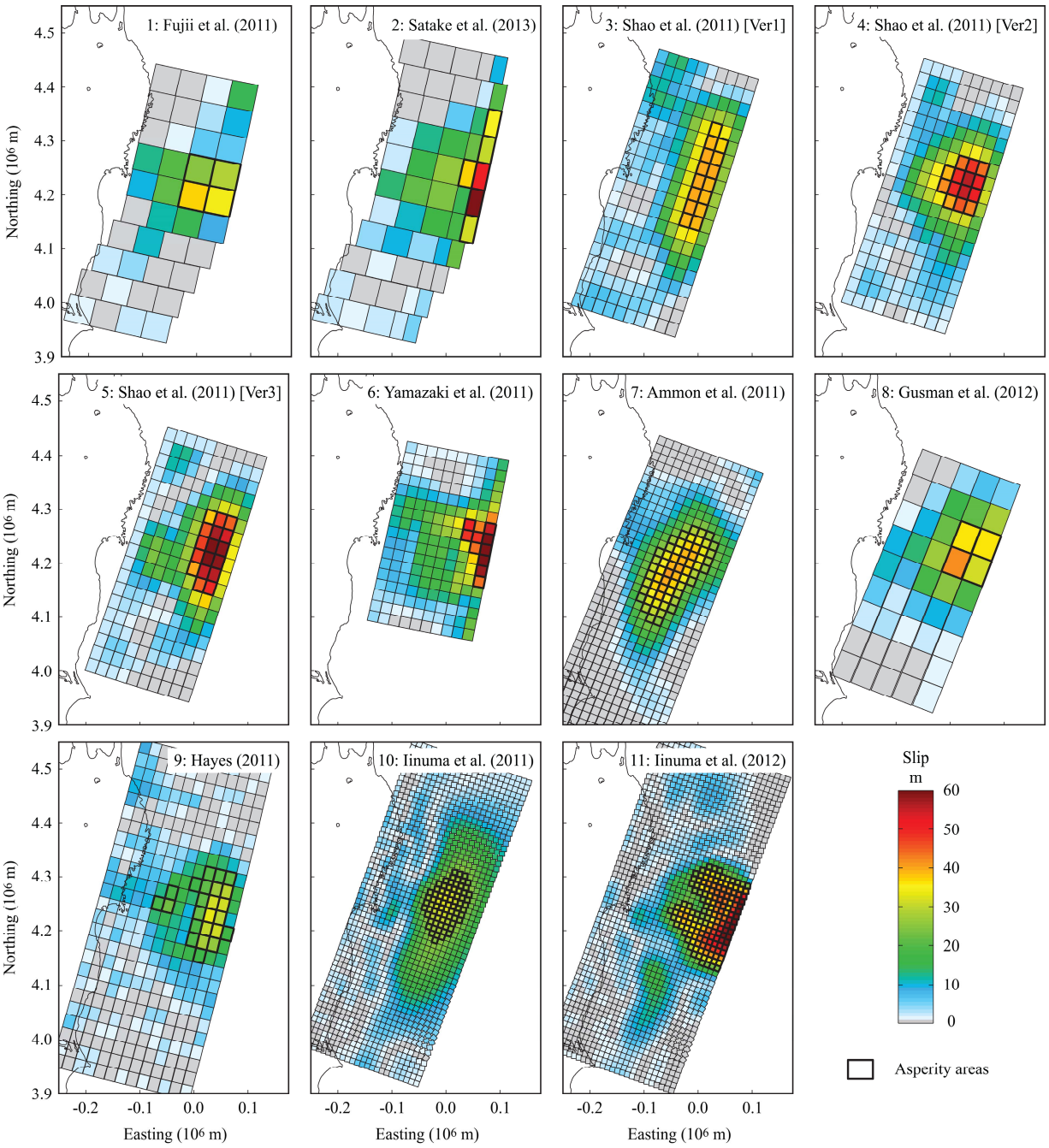

Figure 5. Eleven inversion-based source models. The sub-fault with thick lines represents the asperity area, slip of which is equal to or greater than three times the average slip.

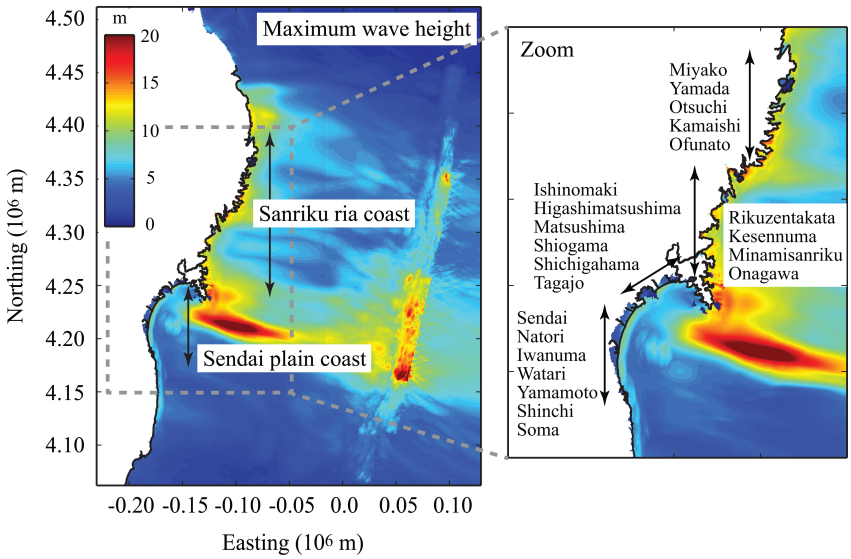

Figure 6. Maximum wave height contour map based on the source model by Satake et al. (2013) and locations of coastal cities and towns in the Tohoku region.

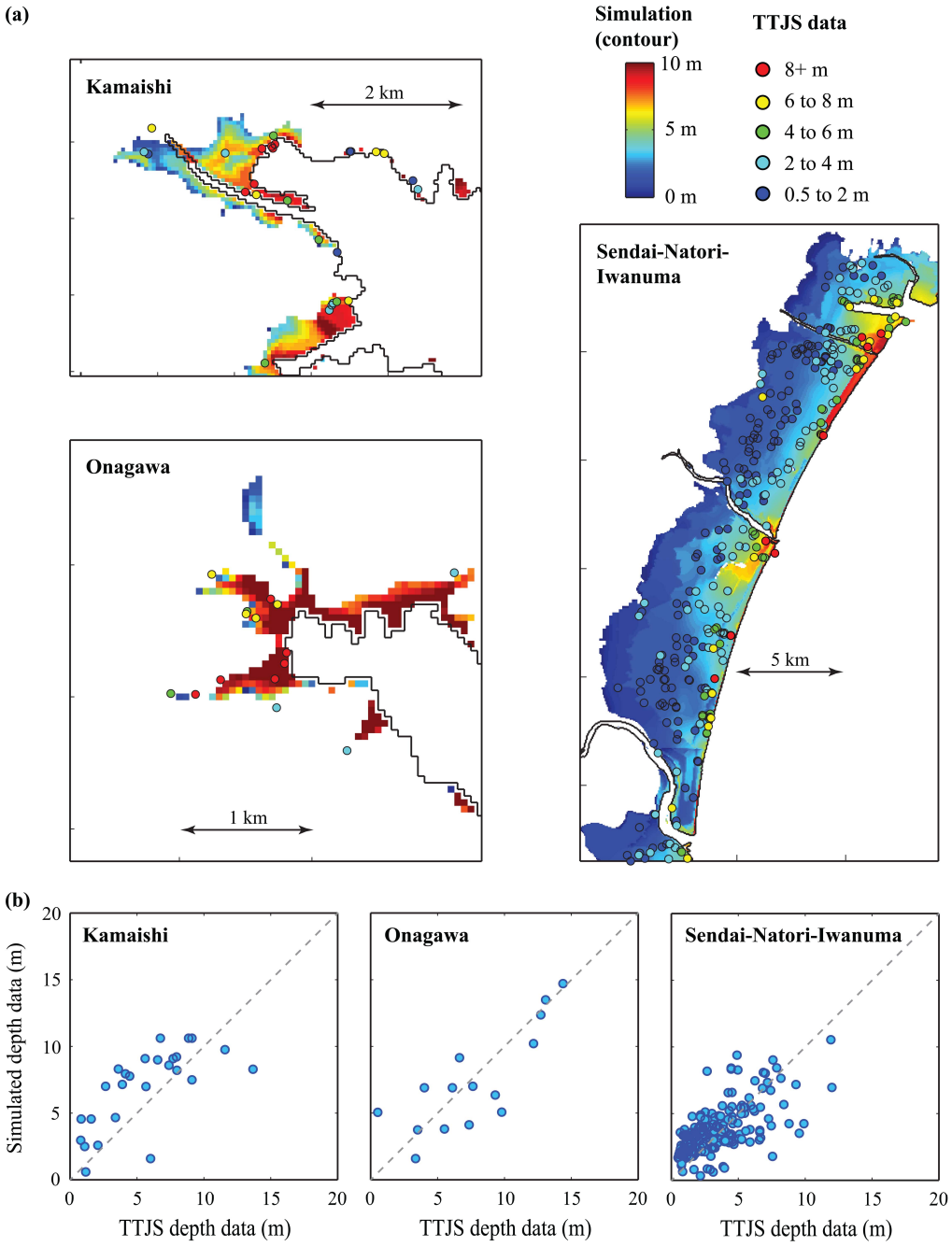

Figure 7. Comparison of tsunami simulation results based on the source model by Satake et al. (2013) with the Tohoku Tsunami Joint Survey (TTJS) data (Mori et al., 2011) in Kamaishi, Onagawa, and Sendai-Natori-Iwanuma: (a) inundation depth contours and (b) scatter plot.

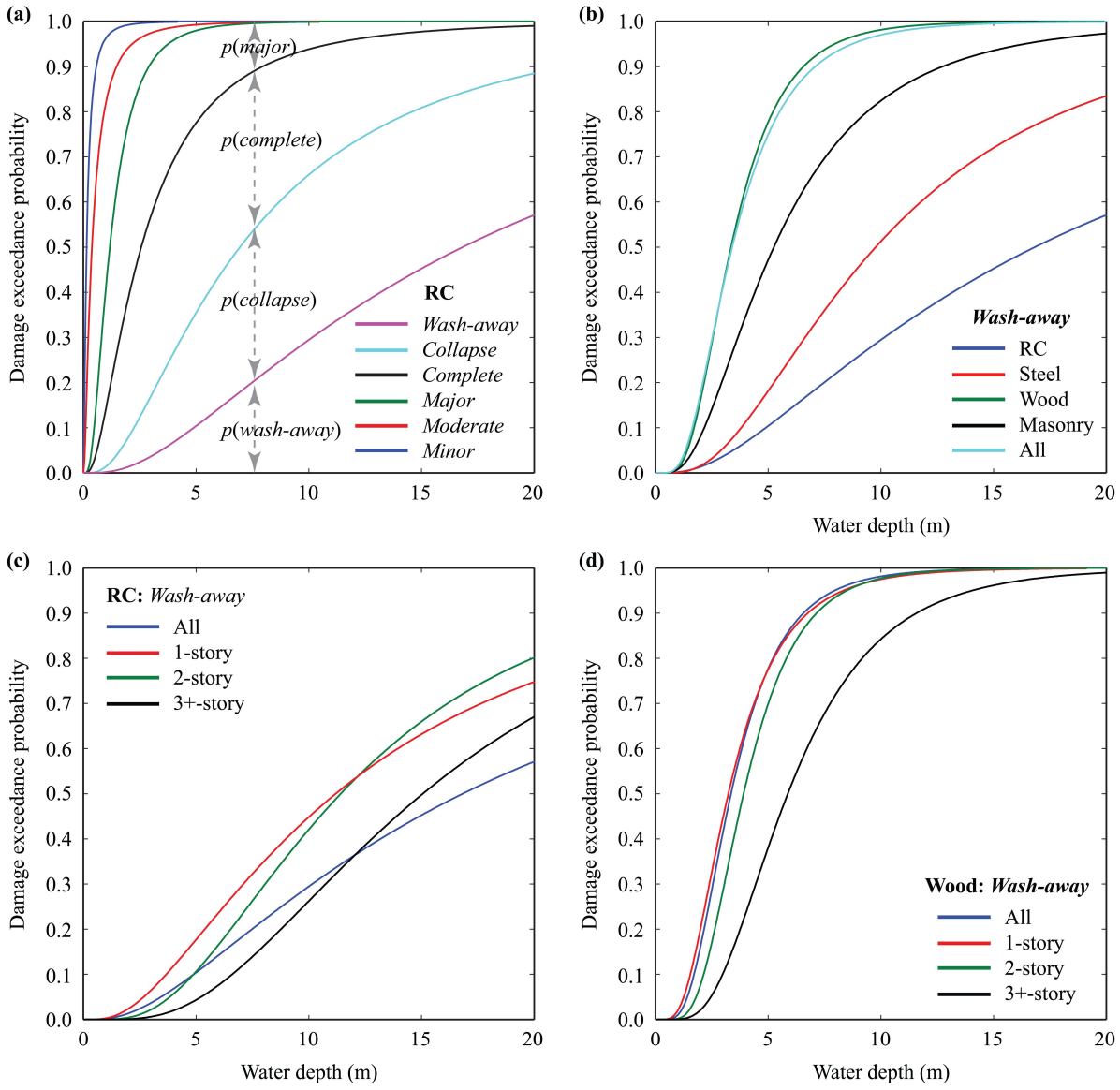

Figure 8. Empirical tsunami fragility curves based on the 2011 Tohoku tsunami damage data (Suppasri et al., 2013a).

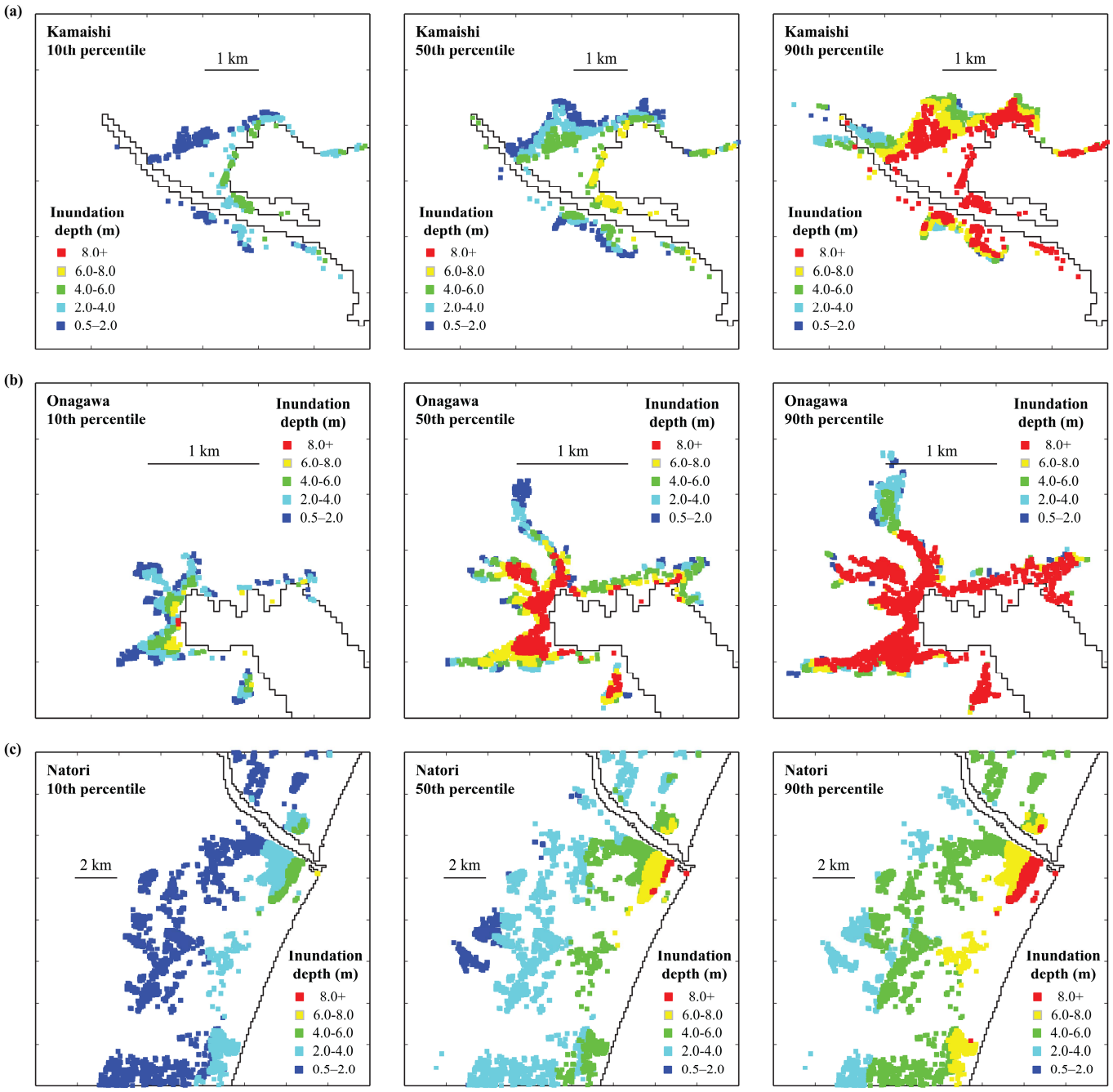

Figure 9. Stochastic inundation depth maps at the 10th, 50th, and 90th percentiles based on the Satake et al. source model: (a) Kamaishi, (b) Onagawa, and (c) Natori.

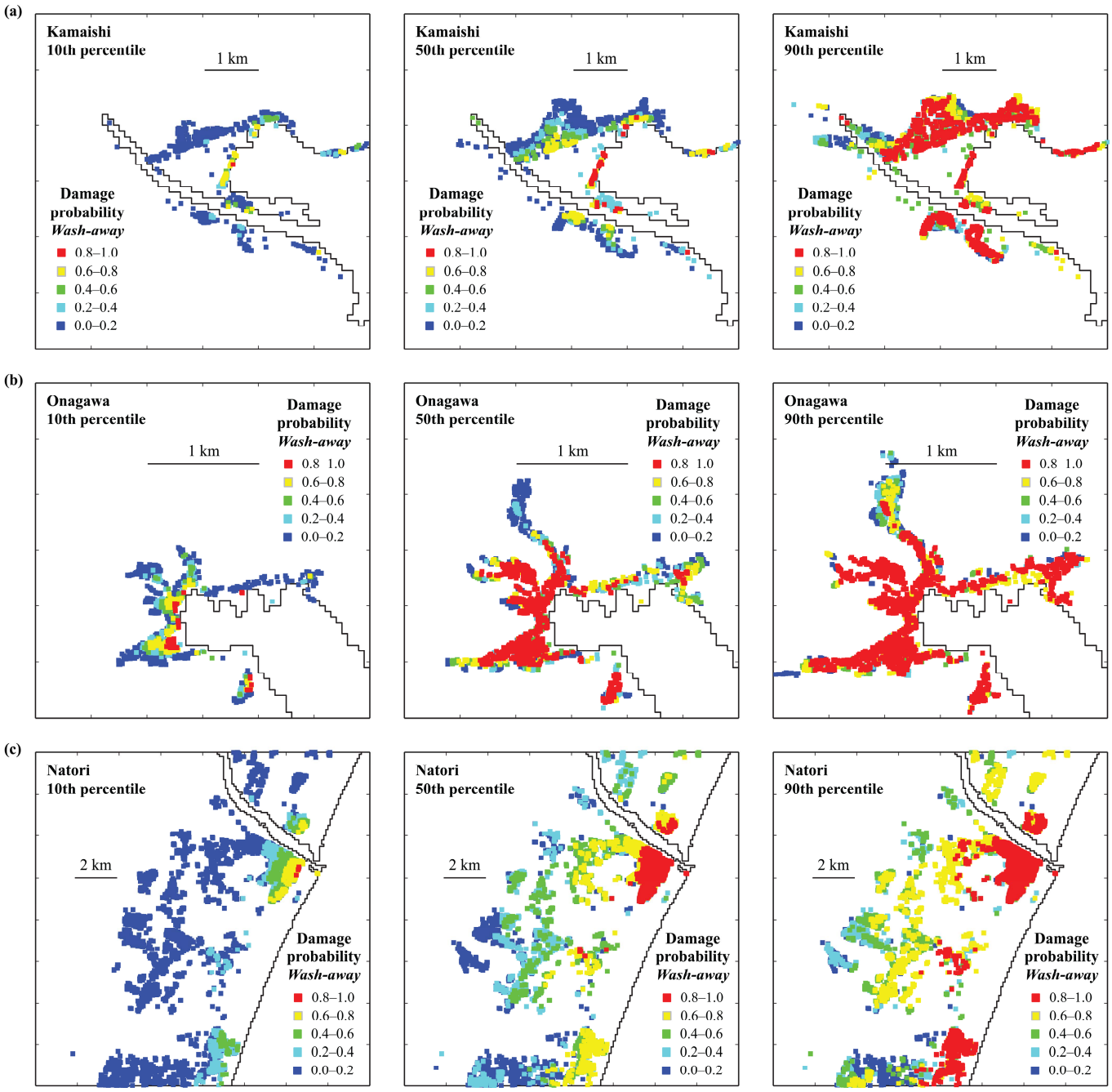

Figure 10. Stochastic *wash-away* damage probability maps at the 10th, 50th, and 90th percentiles based on the Satake et al. source model: (a) Kamaishi, (b) Onagawa, and (c) Natori.

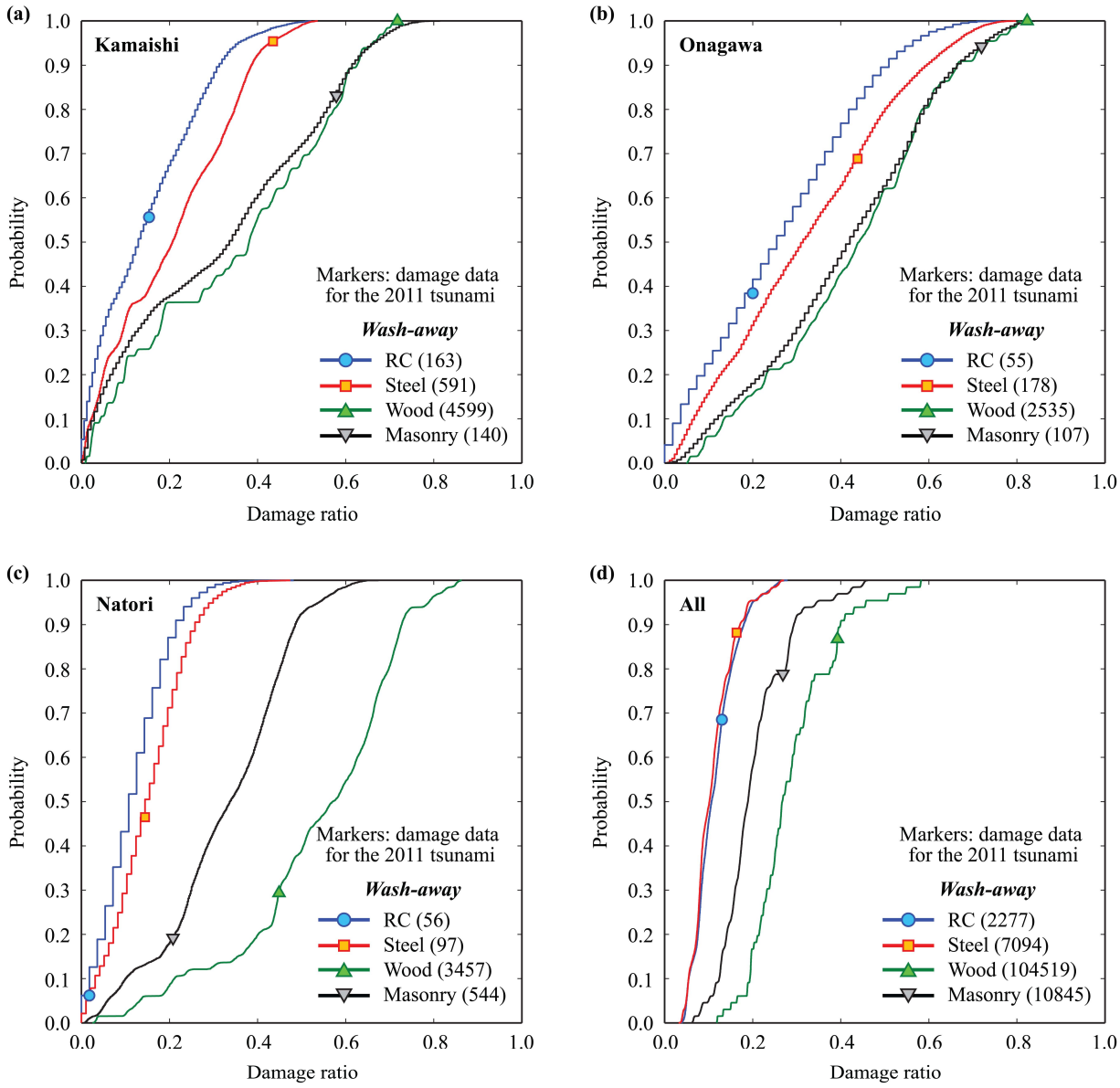

Figure 11. Cumulative distribution functions of the number of buildings in the *wash-away* damage state based on the Satake et al. source model: (a) Kamaishi, (b) Onagawa, (c) Natori, and (d) all cities and towns in the Tohoku region.

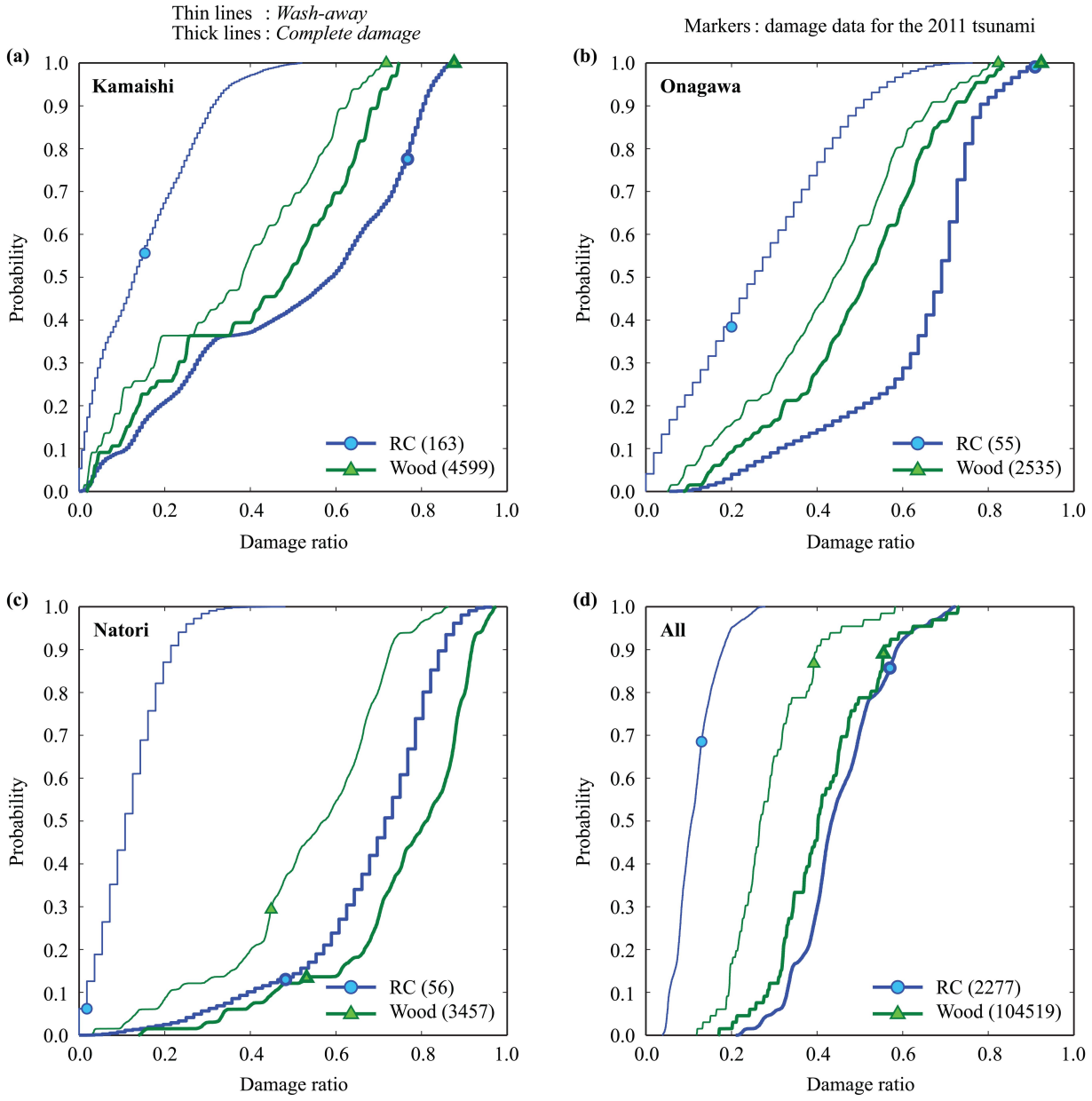

Figure 12. Comparison of cumulative distribution functions of the number of RC/wood buildings in the *wash-away* and *complete damage* states based on the Satake et al. source model: (a) Kamaishi, (b) Onagawa, (c) Natori, and (d) all cities and towns in the Tohoku region.

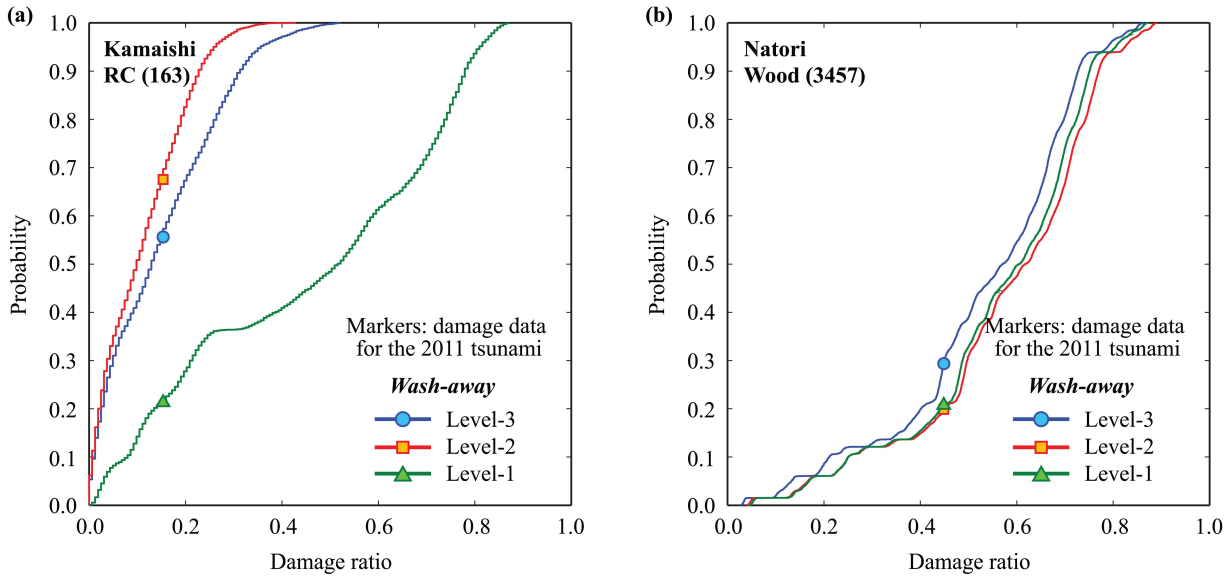

Figure 13. Cumulative distribution functions of the number of buildings in the *wash-away* damage state based on the Satake et al. source model by considering different refinement levels of tsunami fragility models: (a) RC buildings in Kamaishi and (b) wood buildings in Natori.

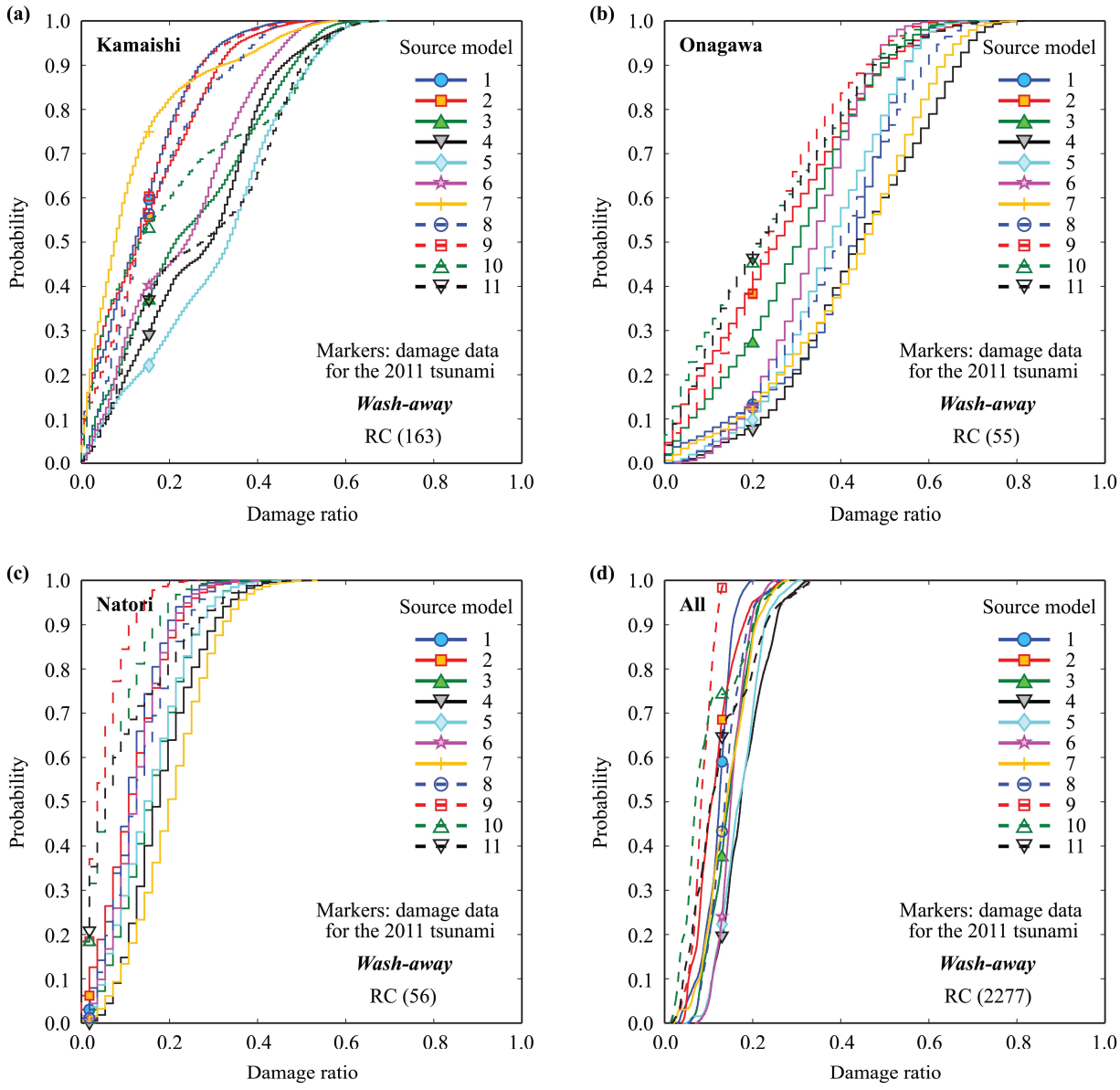

Figure 14. Cumulative distribution functions of the number of RC buildings in the *wash-away* damage state based on the eleven source models (separate curves for individual reference source models): (a) Kamaishi, (b) Onagawa, (c) Natori, and (d) all cities and towns in the Tohoku region.

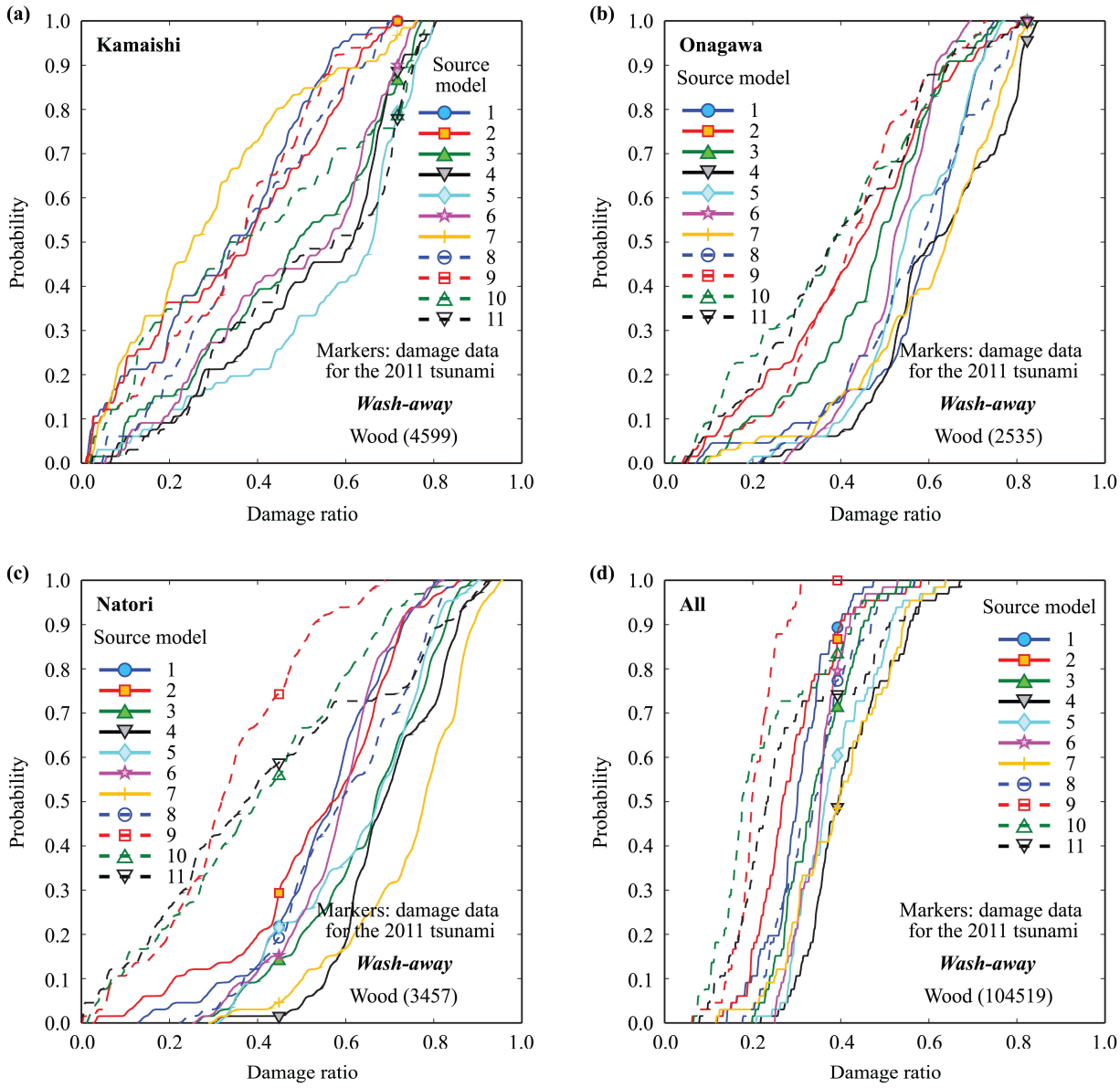

Figure 15. Cumulative distribution functions of the number of wood buildings in the *wash-away* damage state based on the eleven source models (separate curves for individual reference source models): (a) Kamaishi, (b) Onagawa, (c) Natori, and (d) all cities and towns in the Tohoku region.

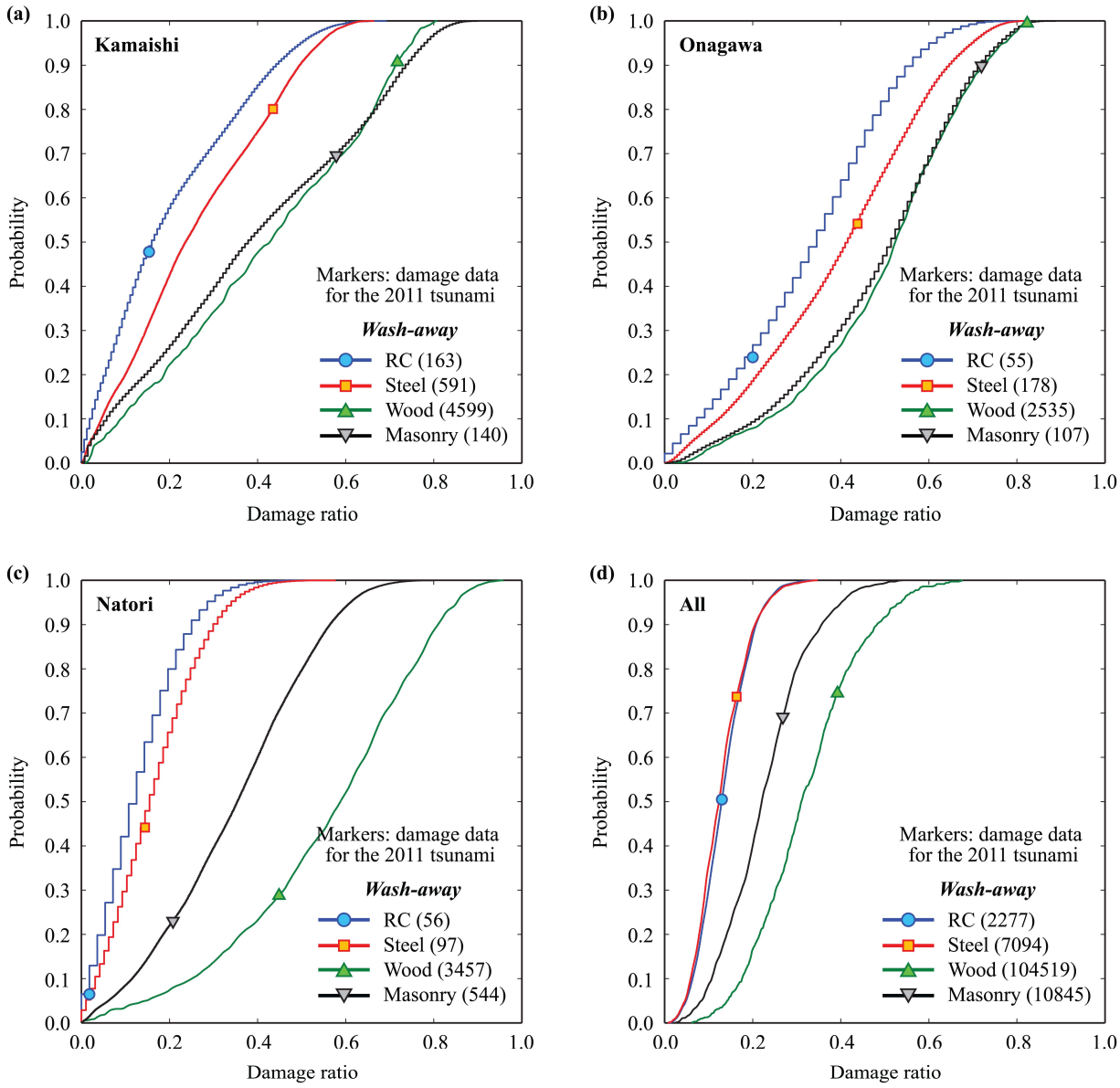

Figure 16. Cumulative distribution functions of the number of buildings in the *wash-away* damage state based on the eleven source models (integrated curves for all reference source models): (a) Kamaishi, (b) Onagawa, (c) Natori, and (d) all cities and towns in the Tohoku region.